



HAL
open science

SOLIS. XII. SVS13-A Class I chemical complexity as revealed by S-bearing species

C. Codella, E. Bianchi, L. Podio, S. Mercimek, C. Ceccarelli, A. López-Sepulcre, R. Bachiller, P. Caselli, N. Sakai, R. Neri, et al.

► **To cite this version:**

C. Codella, E. Bianchi, L. Podio, S. Mercimek, C. Ceccarelli, et al.. SOLIS. XII. SVS13-A Class I chemical complexity as revealed by S-bearing species. *Astronomy and Astrophysics - A&A*, 2021, 654, 10.1051/0004-6361/202141485 . insu-03705277

HAL Id: insu-03705277

<https://insu.hal.science/insu-03705277>

Submitted on 27 Jun 2022

HAL is a multi-disciplinary open access archive for the deposit and dissemination of scientific research documents, whether they are published or not. The documents may come from teaching and research institutions in France or abroad, or from public or private research centers.

L'archive ouverte pluridisciplinaire **HAL**, est destinée au dépôt et à la diffusion de documents scientifiques de niveau recherche, publiés ou non, émanant des établissements d'enseignement et de recherche français ou étrangers, des laboratoires publics ou privés.

SOLIS

XII. SVS13-A Class I chemical complexity as revealed by S-bearing species[★]

C. Codella^{1,2}, E. Bianchi^{2,1}, L. Podio¹, S. Mercimek^{1,3}, C. Ceccarelli², A. López-Sepulcre^{2,4}, R. Bachiller⁵, P. Caselli⁶, N. Sakai⁷, R. Neri⁴, F. Fontani¹, C. Favre², N. Balucani^{8,1,2}, B. Lefloch², S. Viti^{9,10}, and S. Yamamoto^{11,12}

¹ INAF, Osservatorio Astrofisico di Arcetri, Largo E. Fermi 5, 50125 Firenze, Italy
e-mail: claudio.codella@inaf.it

² Univ. Grenoble Alpes, CNRS, Institut de Planétologie et d'Astrophysique de Grenoble (IPAG), 38000 Grenoble, France

³ Università degli Studi di Firenze, Dipartimento di Fisica e Astronomia, Via G. Sansone 1, 50019 Sesto Fiorentino, Italy

⁴ Institut de Radioastronomie Millimétrique, 300 rue de la Piscine, Domaine Universitaire de Grenoble, 38406 Saint-Martin d'Hères, France

⁵ Observatorio Astronómico Nacional (OAN-IGN), Alfonso XII 3, 28014 Madrid, Spain

⁶ Max-Planck-Institut für extraterrestrische Physik (MPE), Giessenbachstrasse 1, 85748 Garching, Germany

⁷ RIKEN Cluster for Pioneering Research, 2-1, Hirosawa, Wako-shi, 351-0198 Saitama, Japan

⁸ Dipartimento di Chimica, Biologia e Biotechnologie, Via Elce di Sotto 8, 06123 Perugia, Italy

⁹ Leiden Observatory, Leiden University, PO Box 9513, 2300 RA Leiden, The Netherlands

¹⁰ Department of Physics and Astronomy, University College London, Gower Street, London, WC1E 6BT, UK

¹¹ Department of Physics, The University of Tokyo, 7-3-1, Hongo, Bunkyo-ku, Tokyo 113-0033, Japan

¹² Research Center for the Early Universe, The University of Tokyo, 7-3-1, Hongo, Bunkyo-ku, Tokyo 113-0033, Japan

Received 7 June 2021 / Accepted 27 August 2021

ABSTRACT

Context. Recent results in astrochemistry have revealed that some molecules, such as interstellar complex organic species and deuterated species, can serve as valuable tools in the investigation of star-forming regions. Sulphuretted species can also be used to follow the chemical evolution of the early stages of a Sun-like star formation process.

Aims. The goal is to obtain a census of S-bearing species using interferometric images towards SVS13-A, a Class I object associated with a hot corino that is rich in interstellar complex organic molecules.

Methods. To this end, we used the NGC 1333 SVS13-A data at 3 mm and 1.4 mm obtained with the IRAM-NOEMA interferometer in the framework of the SOLIS (Seeds of Life in Space) Large Program. The line emission of S-bearing species was imaged and analyzed using local thermodynamic equilibrium (LTE) and large velocity gradient (LVG) approaches.

Results. We imaged the spatial distribution on ≤ 300 au scale of the line emission of ^{32}SO , ^{34}SO , C^{32}S , C^{34}S , C^{33}S , OCS , $\text{H}_2\text{C}^{32}\text{S}$, $\text{H}_2\text{C}^{34}\text{S}$, and NS . The low excitation (9 K) ^{32}SO line traces: (i) the low-velocity SVS13-A outflow and (ii) the fast (up to 100 km s^{-1} away from the systemic velocity) collimated jet driven by the nearby SVS13-B Class 0 object. Conversely, the rest of the lines are confined in the inner SVS13-A region, where complex organics were previously imaged. More specifically, the non-LTE LVG analysis of SO , SO_2 , and H_2CS indicates a hot corino origin (size in the 60–120 au range). Temperatures between 50 K and 300 K, as well as volume densities larger than 10^5 cm^{-3} have been derived. The abundances of the sulphuretted are in the following ranges: $0.3\text{--}6 \times 10^{-6}$ (CS), $7 \times 10^{-9}\text{--}1 \times 10^{-7}$ (SO), $1\text{--}10 \times 10^{-7}$ (SO_2), a few 10^{-10} (H_2CS and OCS), and $10^{-10}\text{--}10^{-9}$ (NS). The $\text{N}(\text{NS})/\text{N}(\text{NS}^+)$ ratio is larger than 10, supporting the assessment that the NS^+ ion is mainly formed in the extended envelope.

Conclusions. The $[\text{H}_2\text{CS}]/[\text{H}_2\text{CO}]$ ratio, once measured at high-spatial resolutions, increases with time (from Class 0 to Class II objects) by more than one order of magnitude (from $\leq 10^{-2}$ to a few 10^{-1}). This suggests that $[\text{S}]/[\text{O}]$ changes along the process of Sun-like star formation. Finally, the estimate of the $[\text{S}]/[\text{H}]$ budget in SVS13-A is 2–17% of the Solar System value (1.8×10^{-5}), which is consistent with what was previously measured towards Class 0 objects (1–8%). This finding supports the notion that the enrichment of the sulphuretted species with respect to dark clouds remains constant from the Class 0 to the Class I stages of low-mass star formation. The present findings stress the importance of investigating the chemistry of star-forming regions using large observational surveys as well as sampling regions on the scale of the Solar System.

Key words. stars: formation – ISM: abundances – ISM: molecules – ISM: individual objects: SVS13-A

1. Introduction

Molecular complexity builds up at each step of the process leading to Sun-like star formation. Searches for exoplanets have shown a broad range of diversity in the planetary systems¹ and

[★] The reduced datacubes are also available at the CDS via anonymous ftp to cdsarc.u-strasbg.fr (130.79.128.5) or via <http://cdsarc.u-strasbg.fr/viz-bin/cat/J/A+A/654/A52>

¹ <https://exoplanets.nasa.gov/>

it is unclear how common a System like our own really is. In this context, the role of the pre-solar chemistry in the formation of the Solar System bodies is not yet understood. A breakthrough question (see e.g., Ceccarelli et al. 2007; Herbst & van Dishoeck 2009; Caselli & Ceccarelli 2012; Jørgensen et al. 2020, and references therein) is to understand whether planetary systems inherited at least part of the chemical composition of the earliest stages of the Sun-like star forming process, such as the prestellar cloud, Class 0 ($\leq 10^5$ yr), Class I ($> 10^5$ yr), and

Class II ($>10^6$ yr) objects. In order to achieve progress in this regard, it is of paramount importance: (i) to observe objects representing all the evolutionary stages of the star forming process sampling regions on a Solar System scale and (ii) to combine high-sensitivity spectral surveys collecting a large number of species and emitting lines to constrain their abundances.

In recent years, ALMA revolutionized our comprehension of planet formation, delivering images of rings and gaps (see e.g., Sheehan & Eisner 2017; Fedele et al. 2018; Andrews et al. 2018) in the dust distribution around objects with an age less than 1 Myr. This clearly supports the fact that planetary formation occurs earlier than what was postulated previously, more specifically already in the Class I phase. This, in turn, stresses the importance of investigating Class I objects as a sort of bridge between the prototellar phase and the protoplanetary disks around Class II young objects. Several projects focused on the chemical complexity of Class I objects have recently been performed, mainly focusing our attention on interstellar small or complex (with at least six atoms) organic molecules or deuteration, using both single-dishes and an interferometer (see e.g., Öberg et al. 2014; Bianchi et al. 2017, 2019a,b, 2020; Bergner et al. 2017, 2019; Le Gal et al. 2020; Yang et al. 2021).

In the dense gas typical of star forming regions, $[S]/[H]$ is far to the value measured in our Solar System (1.8×10^{-5} Anders & Grevesse 1989), given sulphur is depleted by several orders of magnitude (e.g., Tieftrunk et al. 1994; Wakelam et al. 2004a; Phuong et al. 2018; Laas & Caselli 2019; van 't Hoff et al. 2020). In the grains, sulphur is expected to be very refractory, likely in the form of FeS (Kama et al. 2019) or S_8 (Shingledecker et al. 2020), while it is still debated which is the main reservoir on dust mantles. For years, H_2S and possibly OCS have been postulated to be the solution, however, thus far they have never been directly detected in interstellar ices (Boogert et al. 2015), so that it seems that other (not yet identified) frozen species contain the majority of sulphur.

The abundance of gaseous S-bearing species drastically increases in the regions where the species frozen out onto the dust mantles are injected into the gas-phase either due to thermal evaporation in the heated central zone of protostars (e.g., in the Class 0/I hot corinos) or because of gas-grain sputtering and grain-grain shattering in shocked regions (e.g., Charnley et al. 1997; Bachiller et al. 2001; Wakelam et al. 2004a; Codella et al. 2005; Sakai et al. 2014b,a; Podio et al. 2014; Imai et al. 2016; Holdship et al. 2016; Taquet et al. 2020; Feng et al. 2020). In both cases, S-bearing species have proved to be extremely useful in the reconstruction of both the chemical history and dynamics of the studied objects. In addition, S-bearing species have been recently imaged in relatively older protoplanetary disks using CS, SO, H_2S , and H_2CS line emission (e.g., Teague et al. 2018; Booth et al. 2018; Phuong et al. 2018; Le Gal et al. 2019; Loomis et al. 2020; Codella et al. 2020; Garufi et al. 2020, 2021; Podio et al. 2020a,b; Oya & Yamamoto 2020). All these studies (i) have shown that S-bearing species are a powerful tool to follow the evolution of the chemistry until the latest stages of star formation and (ii) call for more studies of S-bearing species towards the Class I protostars, which, as mentioned above, represent a crucial transition from the youngest Class 0 protostars and the more evolved Class II protoplanetary disk sources.

In the present paper, we report a survey of the S-bearing species in the Class I source prototype SVS13-A, observed in the framework of the IRAM-NOEMA SOLIS (Seeds Of Life In Space)² (Ceccarelli et al. 2017). The article is organized as

follows. In Sect. 2, we report the description of target source, SVS13-A. We describe the observations in Sect. 3 and the results in Sect. 4. In Sect. 5, we carry out a non-LTE analysis of the obtained data and derive the physical and chemical parameters of the detected S-bearing in the molecules emitting gas. We discuss the implications of our findings in Sect. 6 and summarize the conclusions of this work in Sect. 7.

2. SVS13-A Class I prototypical source

The SVS13-A object is located in the NGC 1333 cluster, in the Perseus region, at a distance of 299 ± 14 pc (Zucker et al. 2018). SVS13-A is in turn a 0'3 binary source (VLA4A, VLA4B; Anglada et al. 2000; Tobin et al. 2016, 2018), which has thus far not been disentangled using mm-wavelengths observations (e.g., Lefèvre et al. 2017; Maury et al. 2019); located close by ($\sim 4''$) is a third object called VLA3. The three objects are surrounded by a large molecular envelope (Lefloch et al. 1998). The bolometric luminosity of SVS13-A is $\sim 50 L_{bol}$, and it is considered as one of the archetypical Class I sources (at least 10^5 yr, e.g., Chini et al. 1997), having been observed in recent decades at different spectral windows (see e.g., Chini et al. 1997; Bachiller et al. 1998; Looney et al. 2000; Chen et al. 2009; Tobin et al. 2016; Maury et al. 2019, and references therein). SVS13-A is driving an extended molecular outflow (Lefloch et al. 1998; Codella et al. 1999; Sperling et al. 2020; Dionatos et al. 2020), associated with the Herbig-Haro (HH) chain 7–11 (Reipurth et al. 1993) as well as younger flows moving towards southern-eastern directions (Lefèvre et al. 2017).

A hot corino has been revealed towards SVS13-A using deuterated water observed with the IRAM 30-m by Codella et al. (2016) and then imaged by De Simone et al. (2017) using the IRAM PdBI and $HCOCH_2OH$ (glycolaldehyde) emission lines, finding a 90 au diameter. The first iCOMs census of interstellar Complex Organic Species (iCOMs; organic molecules with at least six atoms) has been reported by Bianchi et al. (2019a), thanks to the ASAI (Astrochemical Surveys At IRAM) Large Program (Lefloch et al. 2017) unbiased survey in the IRAM spectral windows. In this context, Bianchi et al. (2017, 2019b) analyzed fractionation and deuteration of a large number of species. Several iCOMs have been also detected by Bellocchi et al. (2020) using high-resolution PdBI observations. Unfortunately, even the interferometric campaigns did not allow the observers to clearly identify which component of the binary system is associated with a rich chemistry, noting only that the emission peak is offset ($\sim 1''.5$ to West) from VLA4A (see also Lefèvre et al. 2017).

3. Observations

The SVS13-A region was observed at 1.4 mm and 3 mm in two different setups (hereafter labelled 5 and 6; see also: Ceccarelli et al. 2017) with the IRAM NOEMA interferometer. The phase center of the obtained images is $\alpha_{2000} = 03^h 29^m 03^s.73$, $\delta_{2000} = +31^\circ 16' 03''.8$.

Setup 6, at 3 mm, was observed in A configuration (1 track) using nine antennas in March 2018. The frequency ranges are 80.2–88.3 GHz and 95.7–103.9 GHz. The shortest and longest projected baselines are 64 m and 760 m, respectively. The field of view is about $60''$, while the largest angular scale (LAS) is $\approx 8''$. Line images were produced by subtracting continuum image, using natural weighting, and restored with a clean beam, for a continuum, of $1''.8 \times 1''.1$ (PA $\approx 41^\circ$). We note that the scope

² <https://solis.osug.fr/>

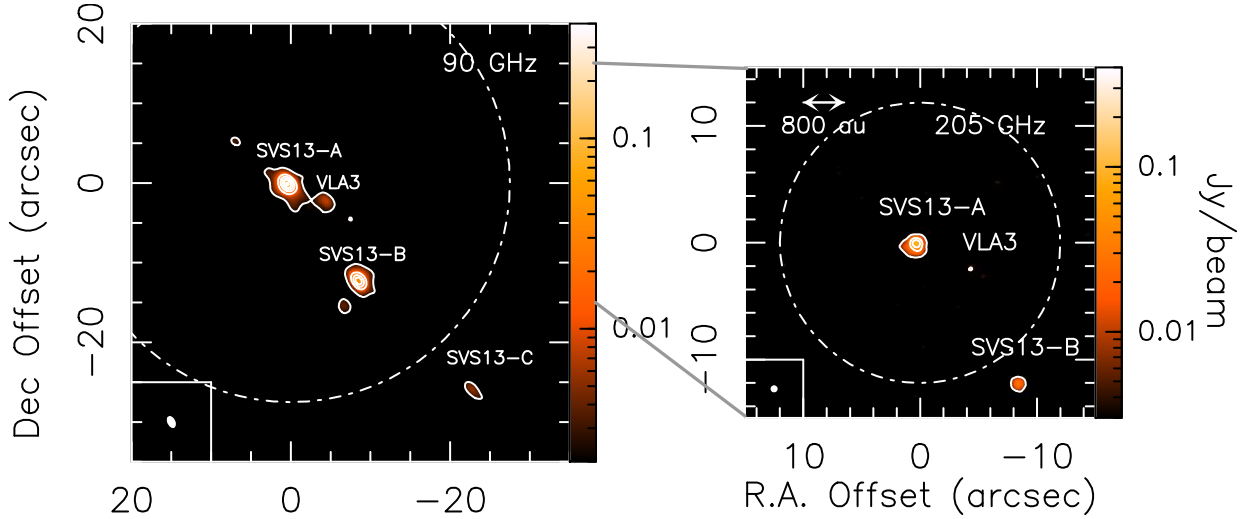


Fig. 1. SVS13-A region as observed in dust continuum emission using IRAM NOEMA. *Left panel:* image at 3 mm (see Sect. 2). Angular offset are with respect to the phase center (see Sect. 3). First contour and steps are 5σ ($1\sigma = 100 \mu\text{Jy}$) and 50σ , respectively. The filled ellipse shows the synthesized beam (HPBW): $1''.6 \times 1''.1$ (PA = 41°). The SVS13-B, SVS13-C, and VLA3 protostars are also labelled. White dashed circle indicate the primary beam: $\sim 55''$. *Right panel:* zoom-in of the inner SVS13-A region as observed in dust continuum at 1.3 mm. First contour and steps are 5σ ($1\sigma = 1 \text{ mJy}$) and 30σ , respectively. Symbols are as in the left panel. The synthesized beam (HPBW) is $0''.6 \times 0''.6$ (PA = -46°), while the primary beam is $24''$.

of the present project is to focus on the hot corino and not the extended emission. The Polyfix correlator was used, with a total spectral band of about 8 GHz, and a spectral resolution of 2 MHz ($\approx 7 \text{ km s}^{-1}$). Setup 5, at 1.4 mm, was observed in A and C configurations (three tracks) using eight antennas in December 2016. The frequency range is 204.0–207.6 GHz. The shortest and longest projected baselines are 24 m and 760 m, respectively, for a field of view of $24''$ and LAS $\sim 9''$. The clean beam is, for the continuum at 1.4 mm, $0''.6 \times 0''.6$ (PA $\approx -46^\circ$). The WideX backend has been used providing a bandwidth of ~ 3.6 GHz with a spectral resolution of ~ 2 MHz ($2.8\text{--}2.9 \text{ km s}^{-1}$). In addition, 320 MHz wide narrowband backends providing a spectral resolution of $\sim 0.9 \text{ km s}^{-1}$ have been used.

For both setups, calibration was carried out following standard procedures, using GILDAS-CLIC³. The bandpass was fixed on 3C84, while the absolute flux was calibrated on LkH α 101, MWC249, and 0333+321. The final uncertainty on the absolute flux scale is $\leq 10\%$ (3 mm) and $\leq 15\%$ (1.4 mm). The phase rms was $\leq 50^\circ$, and the typical precipitable water vapor (pwv) was $\sim 5\text{--}15$ mm. Finally, the system temperature was $\sim 50\text{--}200$ K. The final rms noise in the broadband cubes is $\sim 20\text{--}50 \text{ mJy beam}^{-1}$ (3 mm), and $\sim 700\text{--}1000 \text{ mJy beam}^{-1}$ (1.4 mm).

Figures A.1–A.4 compare the NOEMA-SOLIS spectra with those derived at the same frequency with the IRAM 30-m Lefloch et al. (2018), smoothed to the 2 MHz spectral resolution of the SOLIS data). Red labels indicate the S-bearing species analyzed in this paper (see Table 1). As expected, the single-dish observations are detecting the photons emitted by the multiple components inside the IRAM 30-m HPBW ($25''\text{--}30''$ at 3 mm, and $12''$ at 1.4 mm), such as the cold extended envelope or the large-scale SVS13-A outflow. On the other hand, NOEMA-SOLIS, filtering out the emission at scales larger than $\sim 8''$ is well suited for the analysis of the inner 100 au protostellar region as long as the filtering does not affect the line profile tracing the hot corino.

4. Results

4.1. Continuum images

Figure 1 (left) shows the SVS13-A region as observed in dust continuum emission at 3 mm. Several protostars are detected: SVS13-A (without disentangling the binary components VLA4A and 4B at the present $1''.3$ angular resolution), VLA3, SVS13-B, and, out of the primary beam, also SVS13-C. Figure 1 (right) shows the 1.4 mm map of the inner $30''$ (the primary beam is, in this case, $24''$): while there is a tentative 5σ signature of VLA3, SVS13-A and SVS13-B are clearly detected. Still, at an angular resolution of $0''.6$, the SVS13-A binary system (separated by $0''.3$) is not disentangled.

The J2000 coordinates of the protostars are in agreement with the previous continuum imaging in both cm- and mm-wavelengths (see e.g. Looney et al. 2000; Anglada et al. 2000; Tobin et al. 2018; Maury et al. 2019), namely: SVS13-A: $03^{\text{h}}29^{\text{m}}03^{\text{s}}.757$, $+31^\circ 16' 03''.74$; VLA3: $03^{\text{h}}29^{\text{m}}03^{\text{s}}.386$, $+31^\circ 16' 01''.56$; SVS13-B: $03^{\text{h}}29^{\text{m}}03^{\text{s}}.064$, $+31^\circ 15' 51''.50$; SVS13-C: $03^{\text{h}}29^{\text{m}}01^{\text{s}}.947$, $+31^\circ 15' 37''.71$. Finally, the peak fluxes, for the sources imaged inside the primary beams, are: SVS13-A: $26.6 \pm 0.1 \text{ mJy beam}^{-1}$ (90 GHz), and $94 \pm 1 \text{ mJy beam}^{-1}$ (205 GHz); VLA3: $2.2 \pm 0.1 \text{ mJy beam}^{-1}$ (90 GHz), and $5 \pm 1 \text{ mJy beam}^{-1}$ (205 GHz); SVS13-B: $19.2 \pm 0.1 \text{ mJy beam}^{-1}$ (90 GHz).

4.2. Line images and spectra

We imaged, at both 1.4 mm and 3 mm, a large (32) number of lines of S-bearing species, listed in Table 1. Namely, 4 ^{32}SO (hereafter SO) lines (E_u in the 9–39 K range), 2 ^{34}SO lines (9–19 K), 7 SO_2 lines (37–549 K), 2 $^{34}\text{SO}_2$ lines (55–70 K), 1 C^{32}S (hereafter CS) line (7 K), 1 C^{34}S line (6 K), 1 C^{33}S line (7 K), 3 OCS lines (16–89 K), 9 $\text{H}_2\text{C}^{32}\text{S}$ (hereafter H_2CS) lines (including two pairs blended at the present spectral resolution; 10–244 K), 1 $\text{H}_2\text{C}^{34}\text{S}$ line (48 K), and 1 NS line (27 K). In the following, for sake of clarity, the results of each species will

³ <http://www.iram.fr/IRAMFR/GILDAS>

Table 1. Transitions of S-bearing species detected towards SVS13-A.

Transition	$\nu^{(a)}$ (MHz)	$E_{\text{up}}^{(a)}$ (K)	$S\mu^2^{(a)}$ (D ²)	dv (km s ⁻¹)	rms (mK)	T_{peak} (mK)	V_{peak} (km s ⁻¹)	$FWHM$ (km s ⁻¹)	I_{int} (K km s ⁻¹)
SO									
2 ₂ -1 ₁	86093.95	19	3.5	7.0	22	2765(98)	+8.9(0.2)	9.7(0.5)	27.69(0.23)
2 ₃ -1 ₂	99299.87	9	6.9	6.0	42	4191(42)	+8.7(0.2)	9.4(0.7)	44.30(1.99)
4 ₅ -4 ₄	100029.64	39	0.8	6.0	23	1209(43)	+8.8(0.2)	7.5(0.5)	9.55(0.27)
4 ₅ -3 ₄	206176.01	39	8.9	2.8	920	43142(777)	+8.3(0.2)	9.2(0.2)	422.00(7.38)
³⁴ SO									
2 ₂ -1 ₁	84410.69	19	3.5	7.1	54	296(12)	+9.2(4.2)	7.2(5.1)	2.29(0.68)
2 ₃ -1 ₂	97715.32	9	6.9	6.1	120	436(4)	+8.2(1.1)	9.7(7.0)	4.48(1.20)
SO ₂									
13 _{4,10} -14 _{3,11}	82951.94	123	5.1	7.1	57	751(23)	+7.6(1.7)	9.9(1.5)	7.96(0.68)
8 _{1,7} -8 _{0,8}	83688.09	37	17.0	7.2	72	2071(24)	+7.0(0.3)	10.3(0.5)	22.65(0.94)
32 _{5,27} -31 _{6,26}	84320.88	549	13.5	7.1	40	364(30)	+8.0(2.3)	7.1(6.1)	2.76(0.65)
8 _{3,5} -9 _{2,6}	86639.09	55	3.0	6.9	53	719(22)	+8.1(1.3)	8.9(1.4)	6.82(0.73)
18 _{3,15} -18 _{2,16}	204246.76	181	34.5	2.9	780	12609(160)	+8.2(0.2)	7.6(0.5)	102.64(5.5)
7 _{4,4} -8 _{3,5}	204384.30	65	1.7	2.9	540	2757(210)	+8.0(0.7)	7.9(1.6)	23.09(4.12)
11 _{2,10} -11 _{1,11}	205300.57	70	12.1	2.9	197	11235(230)	+8.7(0.8)	7.3(1.9)	87.28(19.24)
³⁴ SO ₂									
10 _{1,9} -9 _{2,8} ^(b)	82124.35	55	6.5	7.1	160	6998(55)	+9.4(1.2)	8.3(3.2)	63.29(3.03)
12 _{0,12} -11 _{1,11}	204136.23	70	22.7	2.9	1400	5982(780)	+9.1(0.7)	5.4(2.0)	34.56 (9.4)
CS									
2-1	97980.95	7	7.6	6.1	38	5196(12)	+8.6(0.2)	7.0(0.3)	38.72(0.62)
C ³⁴ S									
2-1	96412.95	6	7.6	6.2	45	2088(27)	+7.8(1.4)	6.4(4.8)	14.26(4.38)
C ³³ S									
2-1 $F = 5/2-3/2$ ^(c)	97171.84	7	12.2	6.2	29	388(32)	+8.2(0.5)	8.6(1.2)	3.56(0.33)
OCS									
7-6	85139.10	16	3.5	7.0	36	3787(50)	+8.5(0.4)	7.1(0.2)	28.39(0.34)
8-7	97301.21	21	4.1	6.1	29	5031(86)	+8.6(0.2)	7.6(0.2)	40.73(1.18)
17-16	206745.16	89	8.7	2.8	471	40764(140)	+8.4(0.3)	7.1(0.7)	308.66(4.89)
H ₂ CS									
o-3 _{1,3} -2 _{1,2}	101477.81	23	21.8	5.9	20	1576(12)	+8.6(1.4)	10.0(3.3)	17.12(4.50)
p-3 _{0,3} -2 _{0,2}	103040.45	10	8.2	5.8	33	1603(93)	+8.5(1.3)	6.2(3.3)	10.49(2.26)
p-3 _{2,1} -2 _{2,0}	103051.87	63	4.5	5.8	46	318(18)	+7.8(4.7)	9.9(4.5)	3.79(1.15)
p-6 _{0,6} -5 _{0,5}	205987.86	35	16.3	2.8	159	7702(79)	+8.2(0.2)	7.0(0.2)	57.35(0.56)
p-6 _{4,3} -5 _{4,2} ^(d)	206001.88 ^(d)	244	9.0	2.8	115	15074(260)	+8.8(0.2)	7.3(0.2)	116.65(1.84)
p-6 _{4,2} -5 _{4,1} ^(d)	206001.88 ^(d)	244	9.0						
o-6 _{3,4} -5 _{3,3} ^(d)	206051.94 ^(d)	153	36.6	2.8	161	13512(120)	+7.1(0.8)	7.6(2.1)	108.84(24.75)
o-6 _{3,3} -5 _{3,2} ^(d)	206052.24 ^(d)	153	36.6						
p-6 _{2,4} -5 _{2,3} ^(e)	206158.60 ^(e)	87	14.5	2.8	160	6004(120)	+7.9(0.2)	7.7(0.5)	48.87(0.49)
H ₂ C ³⁴ S									
o-6 _{1,5} -5 _{1,4}	205583.13	48	47.5	0.9	560	3113(190)	+8.6(0.2)	2.7(0.5)	8.91(1.36)
NS									
9/2-7/2 $\Omega = 1/2$ ^(f) l=e	207436.05	27	17.4	2.8	1100	3968(840)	+7.9(0.8)	5.7(1.7)	24.22(6.41)
NS ⁺									
2-1	100198.55	7	8.7	6.0	28	-	-	-	≤ 1 ^(g)

Notes. The Gaussian fit parameters (in T_{MB} scale) refer to the spectra extracted at the emission peak: $\alpha_{2000} = 03^{\text{h}}29^{\text{m}}03^{\text{s}}.75$, $\delta_{2000} = +31^{\circ}16'03''.8$. ^(a)Spectral parameters from the Cologne Database for Molecular Spectroscopy (Müller et al. 2001, 2005) for all the species, with the exception of those of the H₂CS isotopologues, derived from the Jet Propulsion Laboratory (JPL Pickett et al. 1998), and those of NS⁺, from Cernicharo et al. (2018). ^(b)Possible contamination with ¹³CCS emission at 82123.376 MHz ($E_{\text{u}} = 22$ K, $S\mu^2 = 0.7$ D²). ^(c)The C³³S(2-1) line consists of 6 hyperfine components (Bogey et al. 1981; Lovas 2004; Müller et al. 2005) in a 9 MHz frequency interval. The line with the highest $S\mu^2$ is reported (see Fig. 5). ^(d)Lines blended at the present spectral resolution (2 MHz). Possible contamination with CH₃OH emission at 206001.30 MHz ($E_{\text{u}} = 317$ K, $S\mu^2 = 10.2$ D²). ^(e)Contaminated by SO(4₅-3₄) high-velocity emission. ^(f)The 9/2-7/2 $\Omega = 1/2$ line consists of 3 hyperfine components (Lee et al. 1995) in a 0.6 MHz frequency interval. The line with the highest $S\mu^2$ $F = 11/2-9/2$ is reported (see Fig. 5). We give ^(g) 3σ as the upper limit.

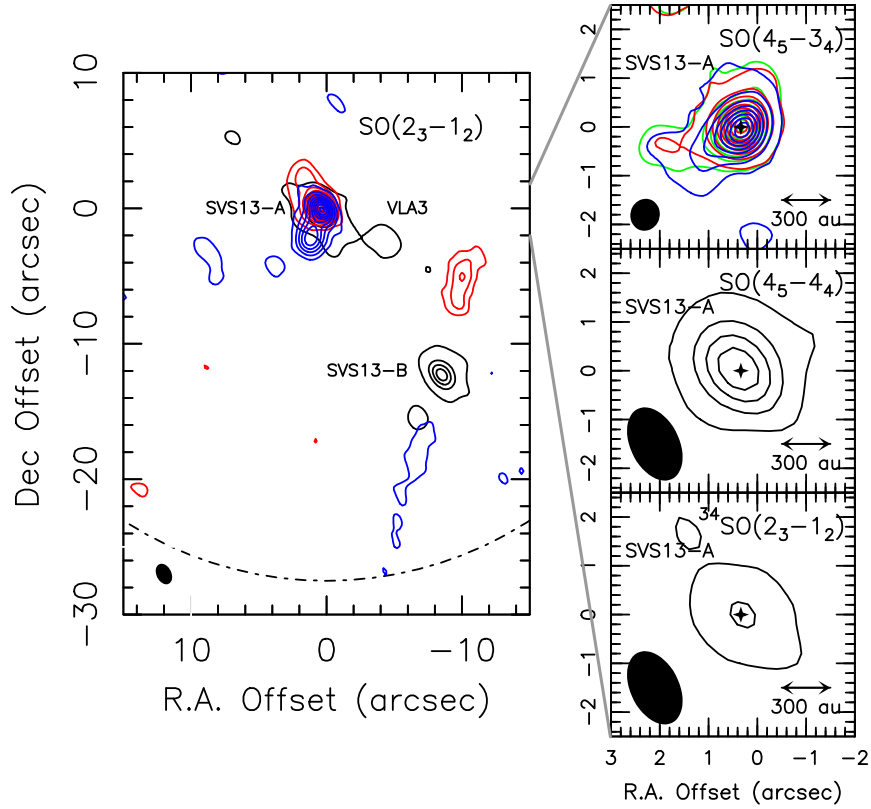


Fig. 2. SVS13-A region as imaged using SO. *Left panel:* spatial distribution of the SO(2_3-1_2) red- and blue-shifted emission overlaid with the 90 GHz continuum map (see Fig. 1). Red-shifted emission maps have been derived by integrating the SO emission from the systemic velocity ($+8.6 \text{ km s}^{-1}$, Chen et al. 2009) up to $+20 \text{ km s}^{-1}$. Blue-shifted image has been obtained by integrating down to -94 km s^{-1} in absolute values). Angular offset are with respect to the phase centre (see Sect. 3). First contour and steps are 3σ and 4σ , respectively. The 1σ value is 5 mJy km s^{-1} and 14 mJy km s^{-1} for the red- and blue-shifted emission, respectively. The filled ellipse shows the synthesized beam (HPBW): $1''.6 \times 1''.1$ (PA = 41°). The SVS13-B protostar is also labelled. White dashed circle indicate the primary beam: $\sim 55''$. *Upper-right panel:* zoom-in of the inner SVS13-A region as observed using the SO(4_5-3_4) emission. Green contours are for the emission in the 3 km s^{-1} around the systemic velocity. Red-shifted emission maps has been derived by integrating the SO emission from the systemic velocity up to $+20 \text{ km s}^{-1}$. Blue-shifted image has been obtained by integrating down to -5 km s^{-1} . First contour and steps are 3σ and 10σ , respectively. The 1σ values are 10 mJy km s^{-1} (systemic velocity), 13 mJy km s^{-1} (red), and 11 mJy km s^{-1} (blue). Symbols are as in the left panel. The black cross indicates the positions of the 205 GHz continuum peak (see Fig. 1). The synthesized beam (HPBW) is $0''.65 \times 0''.58$ (PA = -46°). *Middle-right panel:* zoom-in of the inner SVS13-A region as observed using the SO(4_5-4_4) emission. The whole velocity emitting region has been used (see Fig. 3). First contour and steps are 3σ (9 mJy km s^{-1}) and 10σ , respectively. Symbols are as in the left panel. The synthesized beam (HPBW) is: $1''.6 \times 1''.1$ (PA = 41°). *Bottom-right panel:* zoom-in on the inner SVS13-A region as observed using the $^{34}\text{SO}(2_3-1_2)$ emission. First contour and steps are 3σ (12 mJy km s^{-1}) and 10σ , respectively. Symbols are as in the left panel. The synthesized beam is the same as in the middle-right panel.

be reported separately. The overall picture will be discussed in Sect. 6.

4.2.1. SO

Figure 2 (left) shows the spatial distribution of the low- E_u (9 K) SO(2_3-1_2) emission observed at 86 GHz. The emission peaks are towards SVS13-A and SVS13-B (3 mm continuum drawn in black) and are spatially unresolved. In addition, a contribution from the extended envelope is suggested. Figure 3 reports the SVS13-A spectrum. The used low-spectral resolution (7 km s^{-1}) prevents us from a proper kinematical analysis. However, the peak velocity is centred at the systemic velocity of $+8.6 \text{ km s}^{-1}$ (Chen et al. 2009). By imaging the SO(2_3-1_2) per velocity range, Fig. 2 (left) shows some blue-shifted emission flowing towards the south-east, that is, tracing signatures of the well-known extended ($\gg 8''$) outflow associated with HH7-11 (see e.g., Lefloch et al. 1998; Codella et al. 1999; Lefèvre et al.

2017). In addition, a well collimated (and more compact) bipolar outflow driven by SVS13-B is observed. Very high-velocity emission, up to $+20 \text{ km s}^{-1}$ and down to -94 km s^{-1} , is detected. This outflow, located along the NW–SE direction, had been discovered by Bachiller et al. (1998) using SiO, and recently imaged in the context of the CALYPSO IRAM Large Program Maury et al. (2019) by Podio et al. (2021) in the SiO($5-4$), CO($2-1$), and SO(5_6-4_5) lines. The outflow collimation is consistent with SVS13-B being in an earliest evolutionary stage (Class 0) with respect to SVS13-A (Class I) driving a more extended and less collimated flow.

Moving towards slightly higher excitation lines (up to 39 K), the SO lines observed at 3 mm with $\sim 1''.5$ (450 au) angular resolution appear spatially unresolved and centred on SVS13-A. SVS13-B is detected only through the 2_2-1_1 and 2_3-1_2 lines. On the other hand, the images of the SO lines at 1.4 mm (synthesized beam $\sim 180 \text{ au}$) reveal a structure with a size $\sim 300 \text{ au}$, plausibly associated with the molecular envelope. An elongation

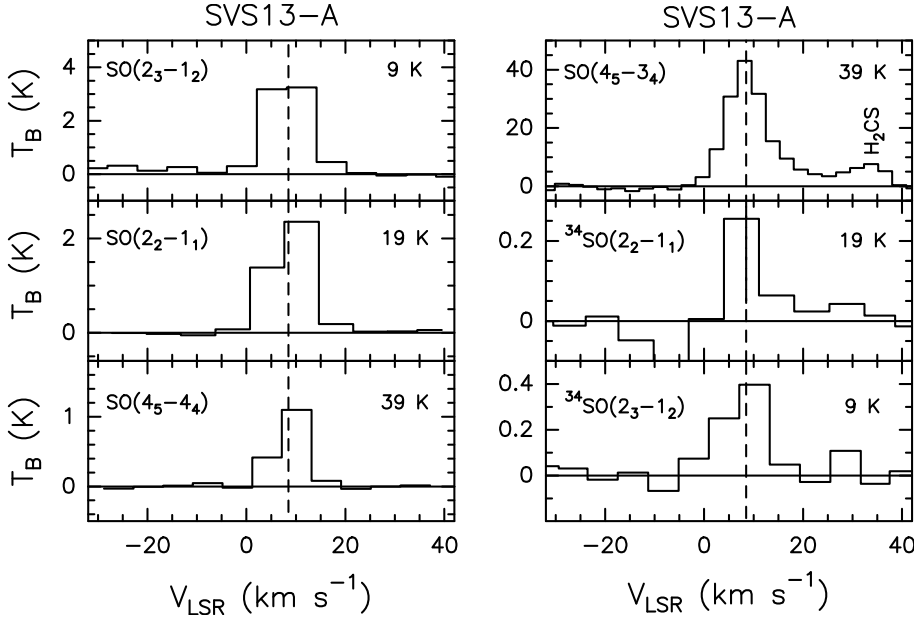


Fig. 3. Observed SO, and ^{34}SO spectra (in T_B scale, see Table 1) extracted at the emission peak: $\alpha_{2000} = 03^{\text{h}}29^{\text{m}}03^{\text{s}}.75$, $\delta_{2000} = +31^{\circ}16'03''.8$. Transitions and corresponding upper level energies are reported. The vertical dashed line stands for the ambient LSR velocity ($+8.6 \text{ km s}^{-1}$, Chen et al. 2009). We note that the p- $\text{H}_2\text{CS}(6_{2,4}-5_{2,3})$ appears close to the $\text{SO}(4_5-3_4)$ profile (see Table 1).

(due to low-velocity blue-shifted emission) towards the blue-shifted outflow SE direction is clearly visible. The $\text{SO}(4_5-3_4)$ line ($E_u = 39 \text{ K}$) profile, observed with a spectral resolution of 2.8 km s^{-1} , has a FWHM line width of 9.2 km s^{-1} .

Finally, the ratio between the integrated fluxes as derived towards SVS13-A of the SO and ^{34}SO 2_3-1_2 or 2_2-1_1 lines is $\sim 10-12$, which, assuming optically thin ^{34}SO emission and $^{32}\text{S}/^{34}\text{S} = 22$ (Wilson & Rood 1994), leads to an SO opacity ~ 1 .

4.2.2. CS

We imaged the $J=2-1$ line emission of the CS, C^{34}S , and C^{33}S isotopologues, emitting in the $96.4-98.0 \text{ GHz}$ spectral range (Table 1). Figure 4 shows how the main isotopologue is tracing the molecular envelope around SVS13-A. The rarer isotopologues are emitting towards the CS emission peak, having a spatially unresolved structure ($\leq 450 \text{ au}$). The spectra corresponding to the CS peak are drawn in Fig. 5. The line ratios observed towards SVS13-A are: $\text{CS}/\text{C}^{34}\text{S} \approx 3$ and $\text{CS}/\text{C}^{33}\text{S} \approx 11$. In turn, assuming the C^{33}S emission to be optically thin and $^{32}\text{S}/^{33}\text{S} = 138$ (Wilson & Rood 1994), this implies optically thick ($\tau \sim 14$) CS emission. The C^{34}S emission results to be moderately thick ($\tau_{\text{C}^{34}\text{S}} \approx 2$).

4.2.3. SO_2

A large number of SO_2 (and $^{34}\text{SO}_2$) lines have been detected at both 3 mm and 1.4 mm , covering a very large range of the upper level energies, from 37 K to 549 K . Figure 6 reports a selection of the spatial distributions of the SO_2 lines, peaking towards SVS13-A. All the spectra are reported in Fig. 7: when observed with a spectral resolution of 2.9 km s^{-1} , the profiles peak close to the systemic velocity ($+8.6 \text{ km s}^{-1}$, Chen et al. 2009), and are $\sim 7-8 \text{ km s}^{-1}$ broad.

Contrary to the cases of SO and CS, the SO_2 emission is spatially unresolved both at 3 mm and 1.4 mm , indicating an emitting size less than 180 au . In other words, there is neither signature of outflows (as for SO) nor of the envelope revealed by SO and CS. The SO_2 and $^{34}\text{SO}_2$ emission is tracing the inner protostellar region. By fitting the position of the brightest SO_2 line

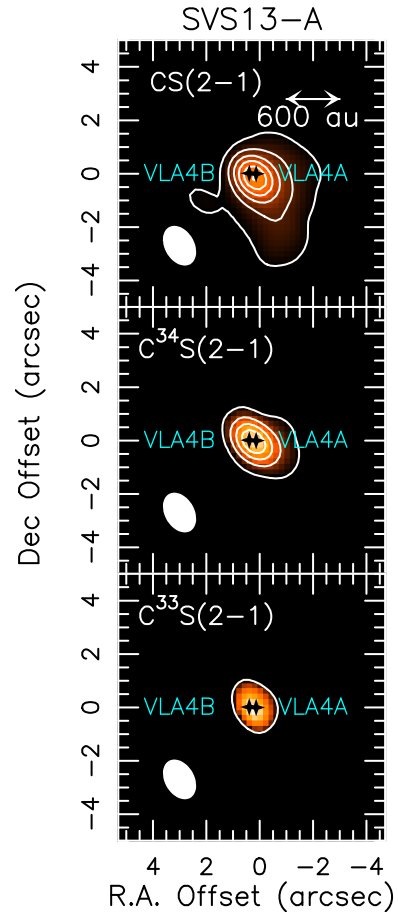


Fig. 4. Spatial distribution of the SVS13-A region obtained using the $J=2-1$ CS (upper panel), C^{34}S (middle), and C^{33}S (bottom) line emission (contours and colour). The whole velocity emitting region has been used (down to -5 km s^{-1} and up to $+25 \text{ km s}^{-1}$, depending on the line, see Fig. 5). Angular offset are respect to the phase centre (see Sect. 3). First contour and steps are 5σ and 10σ , respectively. The 1σ value is 10 mJy km s^{-1} (CS), and 4 mJy km s^{-1} (C^{34}S , C^{33}S). The filled ellipse shows the synthesized beam (HPBW): $1''.6 \times 1''.1$ (PA = 41°). The black crosses indicate the positions of the VLA4A and VLA4B sources as imaged using the VLA array by Tobin et al. (2018).

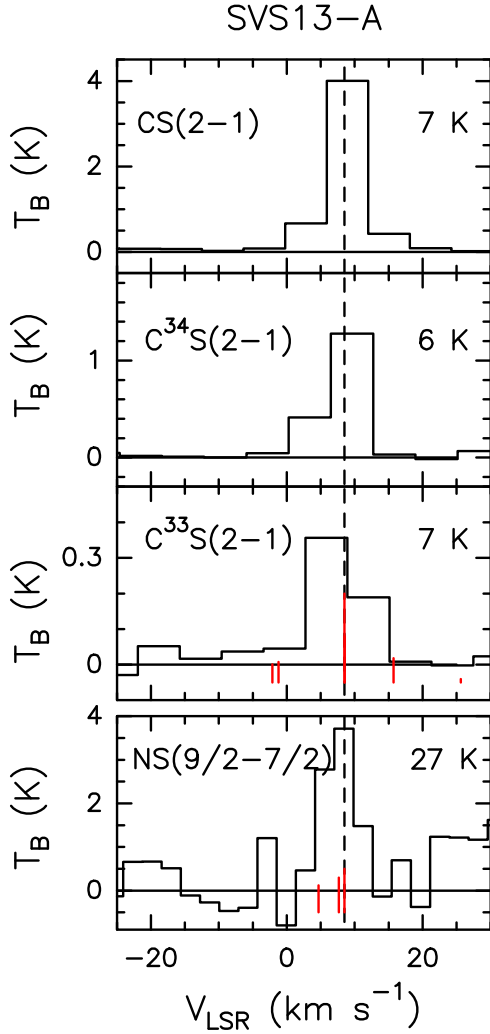


Fig. 5. Observed CS, $C^{34}S$, $C^{33}S$, and NS spectra (in T_B scale, see Table 1) extracted at the emission peak: $\alpha_{2000} = 03^{\text{h}}29^{\text{m}}03^{\text{s}}.75$, $\delta_{2000} = +31^{\circ}16'03''.8$. Transitions and corresponding upper level energies are reported. The vertical dashed line stands for the ambient LSR velocity ($+8.6 \text{ km s}^{-1}$, Chen et al. 2009). The $C^{33}S(2-1)$ line consists of six hyperfine components with $S\mu^2$ in the 0.5–12.2 D^2 range (Bogey et al. 1981; Lovas 2004; Müller et al. 2005) spread on a 9 MHz frequency interval. The vertical red lines (in scales according to their $S\mu^2$) indicated their relative offset in velocity scale with respect to the brightest $F = 5/2-3/2$ line. The NS $9/2-7/2$ $\Omega = 1/2$ line consists of three hyperfine components (Lee et al. 1995) associated with $S\mu^2$ in the 10.9–17.4 D^2 range spread on a 0.6 MHz frequency interval. The vertical red lines (in scales according to their $S\mu^2$) indicated their relative offset in velocity scale with respect to the brightest $F = 11/2-9/2$ line (see Table 1).

(204.2 GHz) using a Gaussian fit in the uv domain⁴, we found $\alpha_{2000} = 03^{\text{h}}29^{\text{m}}03^{\text{s}}.755$, $\delta_{2000} = +31^{\circ}16'03''.782$. The uv fit error is 3 mas. This position lies between the coordinates of the binary components VLA4A and VLA4B (see Fig. 6, right panels), more specifically at $\approx 0''.13$ (39 au) from both protostars. This shift perfectly agrees with what was found using iCOMs emission as imaged with an angular resolution of $0''.4-1''.3$ (at 1.3–3 mm) in the context of the CALYPSO project (De Simone et al. 2017; Belloche et al. 2020). Finally, since we did not detect any common SO_2 and $^{34}SO_2$ lines, we go on to discuss the estimate on

⁴ In the UV domain, the error on centroid positions is the function of the channel signal-to-noise ratio and atmospheric seeing, and is typically much smaller than the beam size.

the SO_2 opacity in Sect. 5 in light of the large velocity gradient (LVG) analysis.

4.2.4. OCS

Figure 8 shows the spatial distribution of the three detected OCS lines. The $J = 7-6$ and $8-7$ transitions fall in the 3 mm band: the emitting size is clearly unresolved with the spatial resolution of $1''.5$. Also the OCS(17–16) line, imaged with a synthesized beam of $0''.6$, is spatially unresolved. The UV analysis leads to a peak coordinates of $\alpha_{2000} = 03^{\text{h}}29^{\text{m}}03^{\text{s}}.754$, $\delta_{2000} = +31^{\circ}16'03''.778$, with an error of 5 mas. This position is consistent with what found using SO_2 , lying between the VLA4A and VLA4B positions. The OCS spectra are reported in Fig. 9: the peak velocity is in agreement with the SVS13-A systemic velocity of $+8.6 \text{ km s}^{-1}$ (Chen et al. 2009). In addition, the OCS(17–16) profile, samples with a 2.8 km s^{-1} , shows a FWHM of 7 km s^{-1} , consistent with those of the SO_2 lines observed at the same angular resolution.

4.2.5. H_2CS

As reported in Table 1, ten H_2CS and $H_2CS^{34}S$ lines, with E_u in the 10–244 K range, have been revealed using both setups at 3 mm and 1.4 mm. Two pairs of SO_2 lines are blended at the present spectral resolution. Figure 10 shows examples of the spatial distributions of the H_2CS lines: as SO_2 and OCS, the emission is peaking towards SVS13-A, being spatially unresolved at both 3 mm and 1.4 mm.

The peak coordinates, according to the uv fit, are $\alpha_{2000} = 03^{\text{h}}29^{\text{m}}03^{\text{s}}.752$, $\delta_{2000} = +31^{\circ}16'03''.786$, with an error of 8 mas, in agreement with the SO_2 and OCS ones. The profiles at the peak emission are shown in Fig. 11. Interestingly, $o\text{-}H_2C^{34}S(6_{1,5}-5_{1,4})$ has been observed with a spectral resolution of 0.9 km s^{-1} , which is certainly an improvement over that of the other lines ($3-7 \text{ km s}^{-1}$). For this line, the profile is well sampled, peaking at the SVS13-A systemic velocity ($+8.6 \text{ km s}^{-1}$, Chen et al. 2009) and with a FWHM of 2.7 km s^{-1} .

4.2.6. NS

The NS(9/2–7/2) $\Omega = 1/2$ line, with $E_u = 27 \text{ K}$, was detected towards SVS13-A. The profile consists of three hyperfine components, blended with the 2.8 km s^{-1} spectral resolution (see Fig. 5). The frequency transition is 207.4 GHz and the corresponding spatial distribution is shown in Fig. 12. The emitting size is unresolved, being less than the $0''.6$ synthesized beam. The emission peaks between the positions of the VLA4A and VLA4B, namely, at $\alpha_{2000} = 03^{\text{h}}29^{\text{m}}03^{\text{s}}.750$, $\delta_{2000} = +31^{\circ}16'03''.808$, with an error of 14 mas. In summary, NS, OCS, SO_2 , H_2CS , once observed with the present spatial resolution ($\sim 100 \text{ au}$), are now tracing the same spatially unresolved region, being consistent with what expected from a chemical enriched region around the protostar(s), that is, the hot corino(s). These findings will be discussed in Sect. 6 in light of the physical parameters derived in Sect. 5.

5. Physical parameters

We analyzed the SO , SO_2 and H_2CS (and their isotopologues) spectra extracted at the emission peak ($\alpha_{2000} = 03^{\text{h}}29^{\text{m}}03^{\text{s}}.75$, $\delta_{2000} = +31^{\circ}16'03''.8$) via the non-local thermodynamic equilibrium (non-LTE) large velocity gradient (LVG) approach using the code `grlvlg` described in Ceccarelli et al. (2003). We assumed a Boltzmann distribution for the H_2 ortho-to-para ratio.

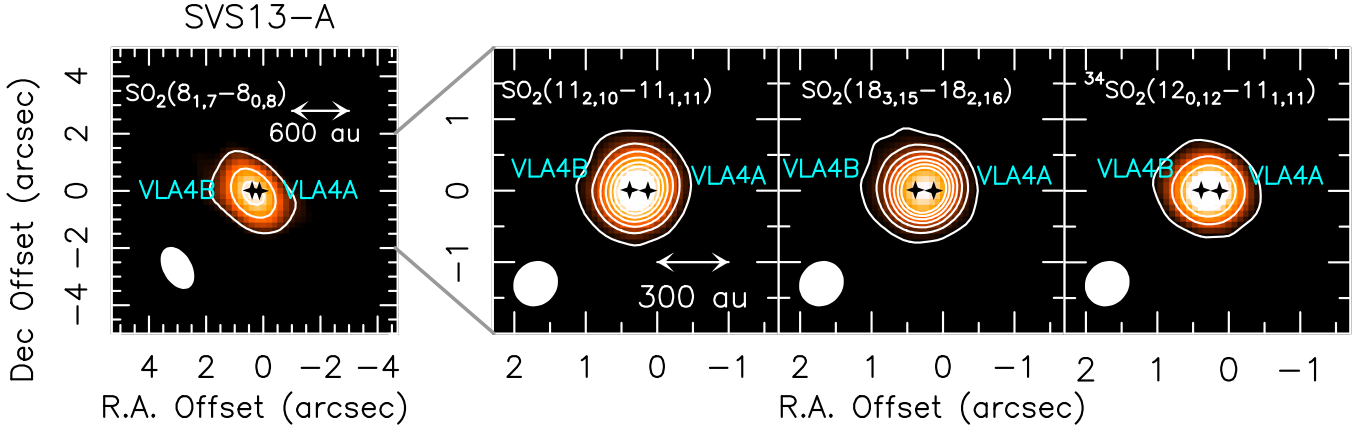


Fig. 6. Spatial distribution (contours and colour) of the SVS13-A region obtained using different SO_2 , and $^{34}\text{SO}_2$ line emission (see Table 1). Angular offset are respect to the phase centre (see Sect. 3). The whole velocity emitting region has been used (from 0 km s^{-1} to $+20 \text{ km s}^{-1}$, see Fig. 7). The $\text{SO}_2(11_{2,10}-11_{1,11})$ profile has been deblended by the CH_3OCHO line fitting the profile with two Gaussians (see Table 1). First contour and steps are 5σ and 10σ , respectively. The 1σ value is: 7 mJy km s^{-1} for $\text{SO}_2(8_{1,7}-8_{0,8})$ (left panel), 14 mJy km s^{-1} for $\text{SO}_2(11_{2,10}-11_{1,11})$, $\text{SO}_2(18_{3,15}-18_{2,16})$, and $^{34}\text{SO}_2(12_{0,12}-11_{1,11})$. The filled ellipse shows the synthesized beam (HPBW): $1''.6 \times 1''.1$ (PA = 41°) for the $\text{SO}_2(8_{1,7}-8_{0,8})$ maps (left panel), and $0''.65 \times 0''.58$ (PA = -46°) for the other images. The black crosses indicate the positions of the VLA4A and VLA4B sources as imaged using the VLA array by Tobin et al. (2018).

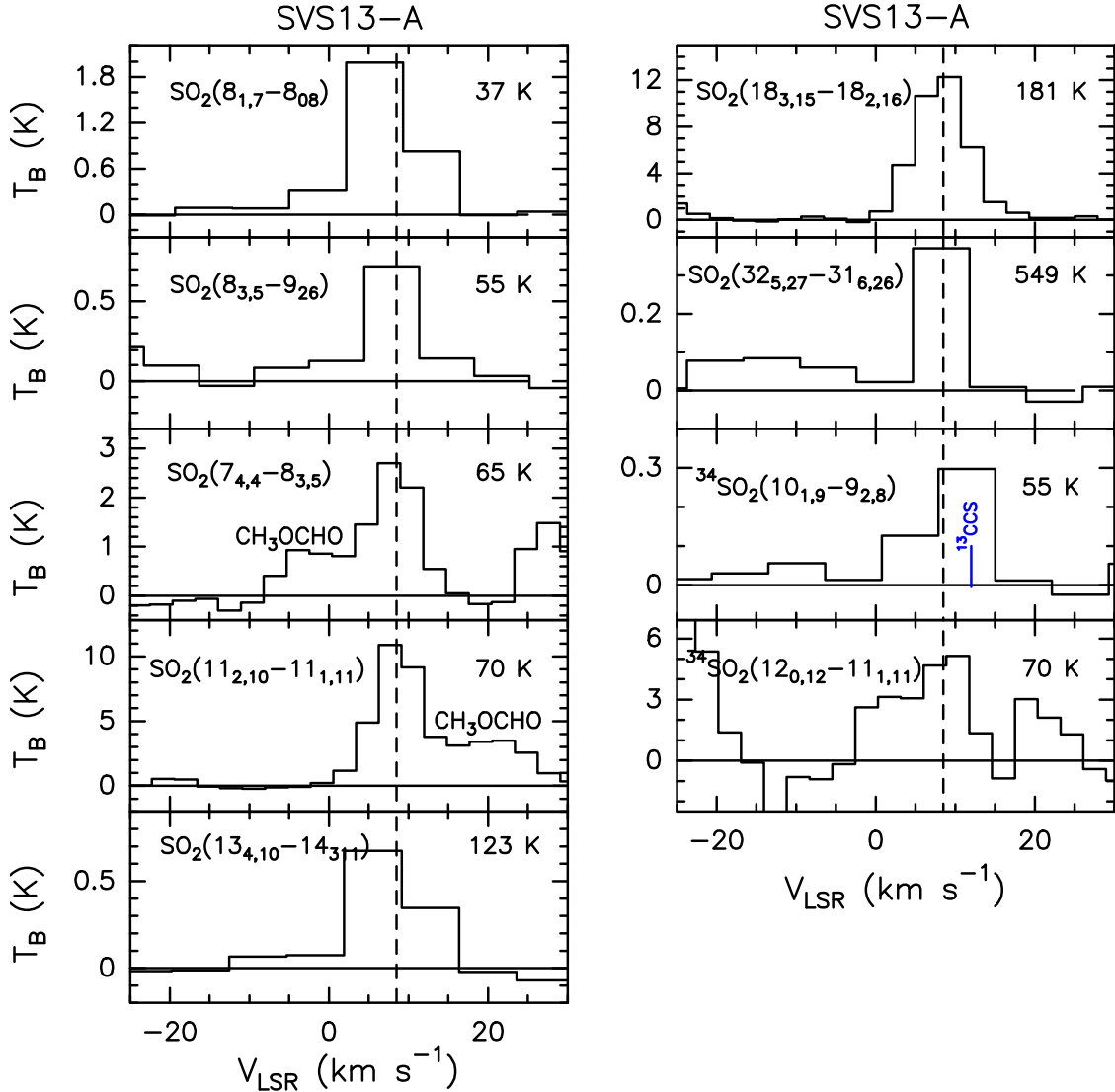


Fig. 7. Observed SO_2 , $^{34}\text{SO}_2$, and $^{33}\text{SO}_2$ spectra (in T_B scale, see Table 1) extracted at the emission peak: $\alpha_{2000} = 03^{\text{h}}29^{\text{m}}03^{\text{s}}.75$, $\delta_{2000} = +31^\circ 16' 03''.8$. Transitions and corresponding upper level energies are reported. The vertical dashed line stands for the ambient LSR velocity ($+8.6 \text{ km s}^{-1}$, Chen et al. 2009). The $^{34}\text{SO}_2$ line at $E_u = 55 \text{ K}$ could be contaminated by ^{13}CCS emission with $E_u = 22 \text{ K}$ (see Table 1).

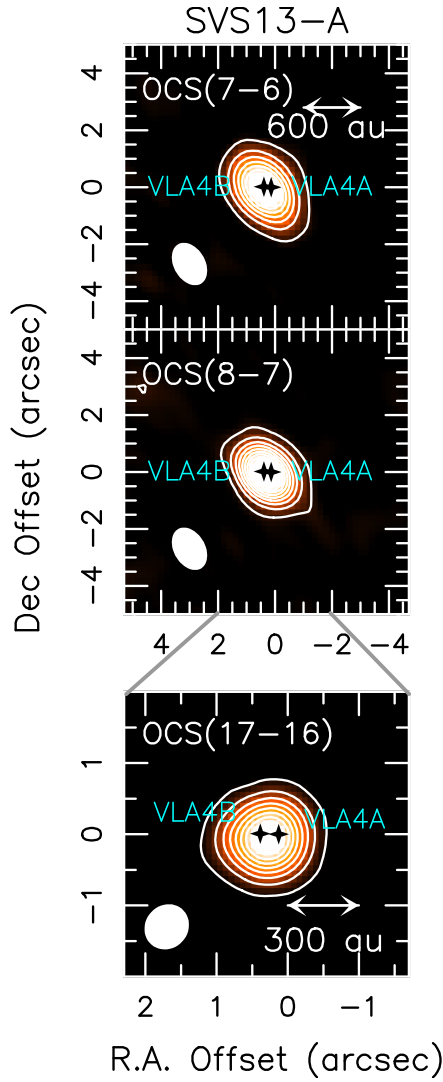


Fig. 8. Spatial distribution of the SVS13-A region obtained using the OCS(7–6) (*upper panel*), OCS(8–7) (*middle*), and OCS(17–16) (*bottom*) line emission (contours and colour). The whole velocity emitting region has been used (from 0 km s^{-1} to $+20 \text{ km s}^{-1}$, see Fig. 9). Angular offsets are shown relative to the phase centre (see Sect. 3). First contour and steps are 5σ and 10σ , respectively. The 1σ value is 5 mJy km s^{-1} ($J=7-6$, and $8-7$), and 26 mJy km s^{-1} ($J=17-16$). The filled ellipse shows the synthesized beam (HPBW): $1''.6 \times 1''.1$ (PA = 41°) for OCS(7–6) and OCS(8–7) and $0''.65 \times 0''.58$ (PA = -46°) for OCS(17–16). The black crosses indicate the positions of the VLA4A and VLA4B sources as imaged using the VLA array by Tobin et al. (2018).

For SO, we used the collisional coefficients with p-H₂ computed by Lique et al. (2007) and retrieved from the BASECOL database (Dubernet et al. 2013). For SO₂, we used the collisional coefficients with ortho- and para-H₂ computed by Balança et al. (2016) and retrieved from the LAMDA database (Schöier et al. 2005). For H₂CS, we used the H₂CO-H₂ collisional coefficients with ortho- and para-H₂ derived by Wiesenfeld & Faure (2013), scaled for the mass ratio, and provided by the LAMDA database (Schöier et al. 2005).

We assumed a semi-infinite slab geometry to compute the line escape probability (Scoville & Solomon 1974) and assumed a line width equal to 8 km s^{-1} . We used the $^{32}\text{S}/^{34}\text{S}$ equal to 22 (Wilson & Rood 1994), and an H₂CS ortho-to-para ratio

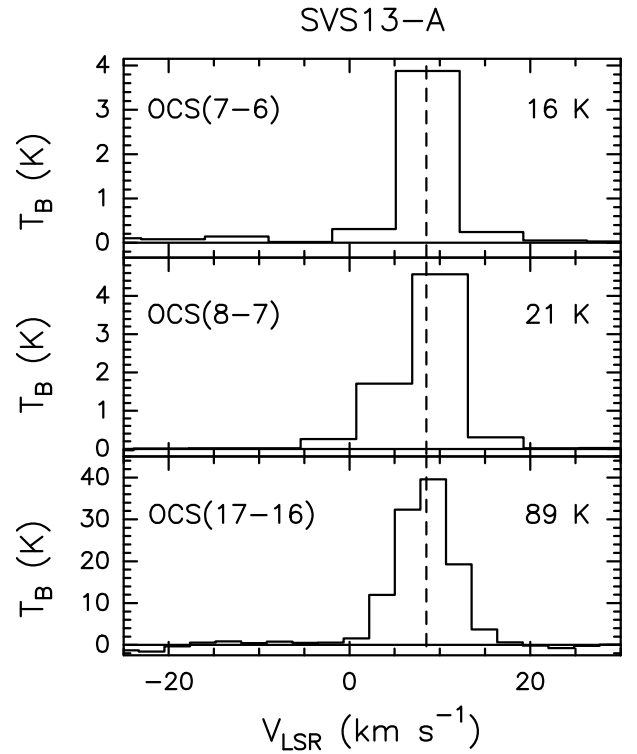


Fig. 9. Observed OCS spectra (in T_B scale, see Table 1) extracted at the emission peak: $\alpha_{2000} = 03^{\text{h}}29^{\text{m}}03^{\text{s}}.75$, $\delta_{2000} = +31^\circ 16' 03''.8$. Transitions and corresponding upper level energies are reported. The vertical dashed line stands for the ambient LSR velocity ($+8.6 \text{ km s}^{-1}$, Chen et al. 2009).

equal to 3. Finally, the errors on the observed line intensities have been obtained adding the spectral r.m.s. to the uncertainties due to calibration (see Sect. 3). We ran large grids of models varying the kinetic temperature (T_{kin}) from 20 to 500 K, the volume density (n_{H_2}) from 10^4 cm^{-3} to 10^9 cm^{-3} , the emitting sizes from $0''.1$ to $30''$ and the SO, SO₂, and H₂CS column densities from 10^{15} cm^{-2} to 10^{21} cm^{-2} . The best fit for each species is obtained by simultaneously minimizing the difference between the predicted and observed integrated intensities of both used isotopologues (e.g., SO and ^{34}SO ; SO₂ and $^{34}\text{SO}_2$; H₂CS, and H₂C³⁴S).

The results obtained for SO show a best solution, characterized by $\chi^2 \approx 2$, with a total column density N_{SO} of 10^{17} cm^{-2} , a kinetic temperature T_{kin} equal to 280 K, and the volume density n_{H_2} being 10^8 cm^{-3} . The size is $0''.3$ (90 au). The line opacities lies between 0.1 and 1.4. If we consider an uncertainty of 1σ , which corresponds to a probability of 30% to exceeding χ^2 , we have $T_{\text{kin}} \geq 150 \text{ K}$, $n_{\text{H}_2} \geq 6 \times 10^6 \text{ cm}^{-3}$, $N_{\text{SO}} = 0.2-3 \times 10^{17} \text{ cm}^{-2}$, and sizes in the $0''.2-0''.5$ range.

The analysis of SO₂ leads to a best solution ($\chi^2 \approx 3$) with the $N_{\text{SO}_2} = 10^{18} \text{ cm}^{-2}$, $T_{\text{kin}} = 210 \text{ K}$, and 10^8 cm^{-3} . The size is $0''.2$ (~ 60 au). The line emission is moderately thick, with an opacity between 0.30 and 4.5. Once we considered the uncertainty of 1σ , we could obtain $T_{\text{kin}} \approx 100-300 \text{ K}$, and $n_{\text{H}_2} \geq 5 \times 10^6 \text{ cm}^{-3}$, $N_{\text{SO}_2} = 0.3-3 \times 10^{18} \text{ cm}^{-2}$, and a size between $0''.1$ and $0''.3$.

The best fit obtained for H₂CS, identified by $\chi^2 \approx 0.1$, indicates the total column density equal to $2 \times 10^{15} \text{ cm}^{-2}$, a size of $0''.4$ (120 au), the kinetic temperature $T_{\text{kin}} = 100 \text{ K}$, and the volume density $n_{\text{H}_2} = 2 \times 10^5 \text{ cm}^{-3}$. The line opacities are all in the 0.04–0.4 range but that of the $6_{0,6}-5_{0,5}$ para line which is

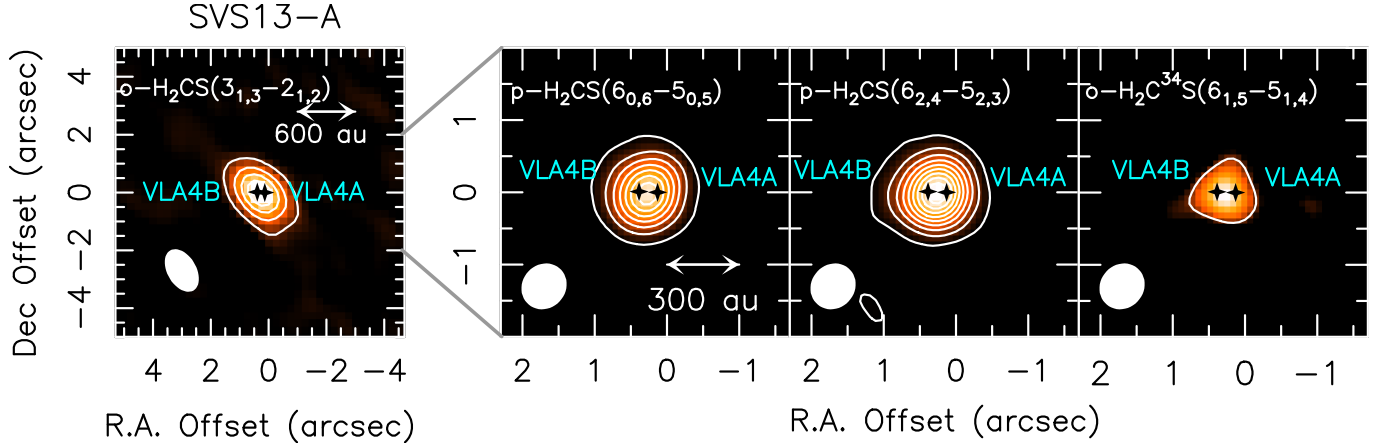


Fig. 10. Spatial distribution (contours and colour) of the SVS13-A region obtained using different H₂CS, and H₂C³⁴S line emission (see Table 1). The whole velocity emitting region has been used (from 0 km s⁻¹ to +20 km s⁻¹, see Fig. 11). The p-H₂CS(6_{2,4}-5_{2,3}) emission has been deblended from the SO emission (see Table 1) applying two Gaussian profiles. Angular offset are relative to the phase centre (see Sect. 2). First contour and steps are 5σ and 10σ, respectively. The 1σ values (from left to right) are 5, 13, 11, and 9 mJy km s⁻¹, respectively. The filled ellipse shows the synthesized beam (HPBW): 1′.6 × 1′.1 (PA= 41°) for the o-H₂CS(3_{1,3}-2_{1,2}) line (*left panel*), and 0′.65 × 0′.58 (PA= -46°) for the p-H₂CS(6_{0,6}-5_{0,5}), p-H₂CS(6_{2,4}-5_{2,3}), and o-H₂C³⁴S(6_{1,5}-5_{1,4}) lines (*middle and right panels*). The black crosses indicate the positions of the VLA4A and VLA4B sources as imaged using the VLA array by Tobin et al. (2018).

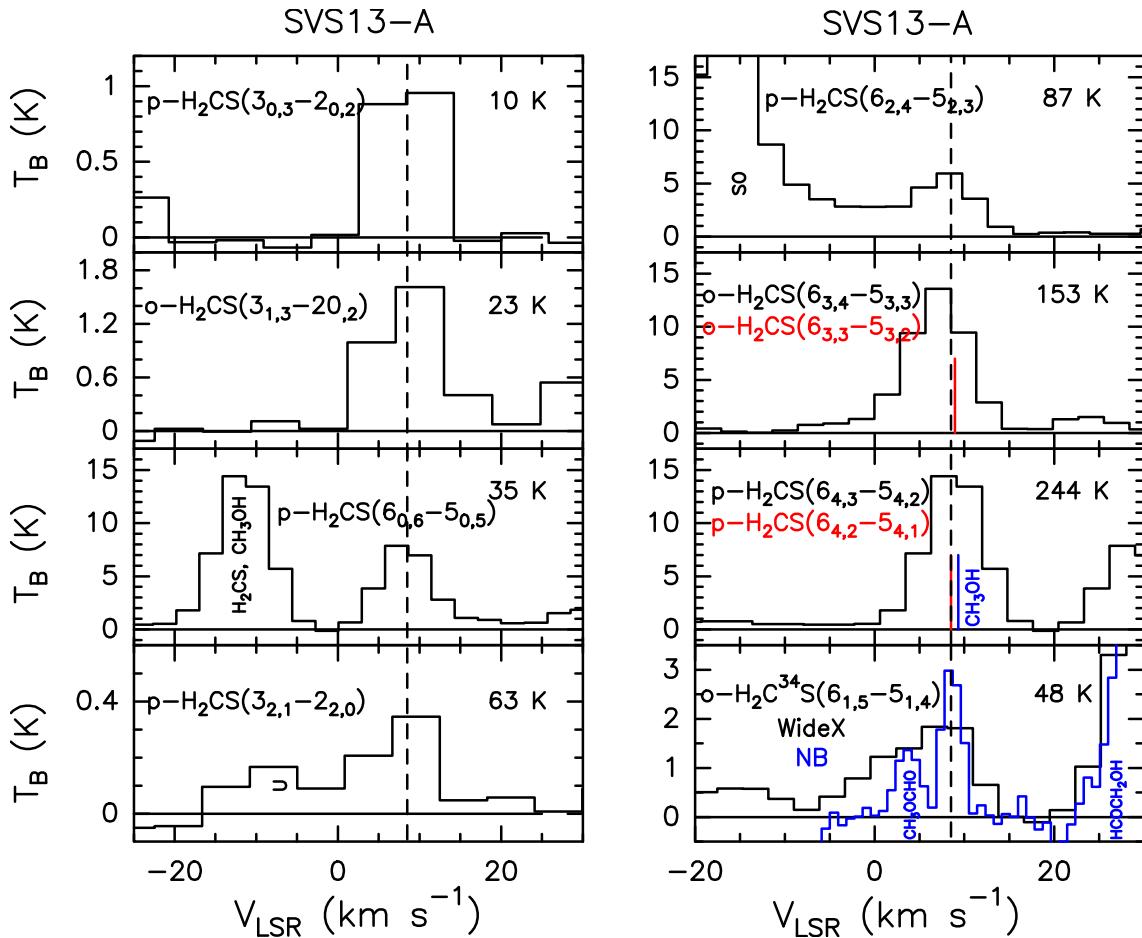


Fig. 11. Observed H₂CS, and H₂C³⁴S spectra (in T_B scale, see Table 1) extracted at the emission peak: $\alpha_{2000} = 03^{\text{h}}29^{\text{m}}03^{\text{s}}.75$, $\delta_{2000} = +31^{\circ}16'03''.8$. Transitions and corresponding upper level energies are reported. The vertical dashed line stands for the ambient LSR velocity (+8.6 km s⁻¹, Chen et al. 2009). Red labels and red vertical segments denote two H₂CS profiles with the same E_u value and blended at the present spectral resolution (Table 1). The black vertical labels indicate that the line is reported in another panel of the present figure. The H₂CS doublets at $E_u = 244$ K could be contaminated by CH₃OH emission with $E_u = 317$ K (see Table 1). The H₂C³⁴S(6_{1,5}-5_{1,4}) profile has been observed using both low- (black histogram) and high-spectral (blue) backends (see Sect. 2: labelled WideX and NB, respectively).

Table 2. 1σ confidence level (range) from the Non-LTE LVG Analysis of the SO, SO₂, and H₂CS lines towards SVS13-A as imaged with NOEMA.

Species	N_{tot} (cm ⁻²)	n_{H_2} (cm ⁻³)	T_{kin} (K)	Size (arcsec)	$X_{\text{H}_2}^{(a)}$
SO	$0.2\text{--}3 \times 10^{17}$	$\geq 6 \times 10^6$	≥ 150 K	$0''.2\text{--}0''.5$	$7 \times 10^{-9}\text{--}1 \times 10^{-7}$
SO ₂	$0.3\text{--}3 \times 10^{18}$	$\geq 5 \times 10^6$	100–300	$0''.1\text{--}0''.3$	$1\text{--}10 \times 10^{-7}$
H ₂ CS	$0.7\text{--}2 \times 10^{15}$	$\geq 10^5$	≥ 50 K	$0''.2\text{--}0''.8$	$2\text{--}7 \times 10^{-10}$
	N_{tot} (cm ⁻²)	n_{H_2} (cm ⁻³)	T_{rot} (K)	Size (arcsec)	$X_{\text{H}_2}^{(a)}$
OCS ^(b)	$1\text{--}2 \times 10^{15}$	–	70–170	$0''.3^{(b)}$	$3\text{--}7 \times 10^{-10}$
CS ^(c)	$0.8\text{--}17 \times 10^{18}$	–	37.5 ^(d) –300	$0''.3^{(c)}$	$0.3\text{--}6 \times 10^{-6}$
NS ^(c)	$1\text{--}6 \times 10^{15}$	–	37.5 ^(d) –300	$0''.3^{(c)}$	$0.2\text{--}3 \times 10^{-9}$
NS ⁺ ^(e)	$\leq 8 \times 10^{14}$	–	37.5 ^(d) –300	$0''.3^{(c)}$	$\leq 3 \times 10^{-10}$
H ₂ S ^{(c),(e)}	$0.5\text{--}1 \times 10^{18}$	–	37.5 ^(d) –300	$0''.3^{(c)}$	$2\text{--}4 \times 10^{-7}$

Notes. The OCS, CS, and NS column densities, derived assuming LTE conditions, are also reported. The last row with H₂S, is based on IRAM 30-m data at 1.4 mm. The last column is for the abundance with respect to H₂. ^(a)We assume $N_{\text{H}_2} = 3 \times 10^{24}$ cm⁻² (Chen et al. 2009). ^(b)Estimate derived using the RD approach, and assuming a source size of $0''.3$ following the SO, SO₂, and H₂CS LVG analysis. ^(c)Estimates derived using one line, and assuming: (i) a source size of $0''.3$, and a temperature in the 37.5–300 K range (from LVG analysis of SO, SO₂, and H₂CS). For CS, we took into account the line opacity of 14 derived from the comparison with the emission of C³⁴S and C³³S. ^(d)For T_{rot} we conservatively used a lower limit of 37.5 K, according to the partition function tabulated in the Jet Propulsion Laboratory (JPL, Pickett et al. 1998) database. ^(e)Estimated based on the $2_{2,0}\text{--}2_{1,1}$ line observed with a HPBW = $11''$ using the IRAM 30-m antenna (see Sect. 6.4).

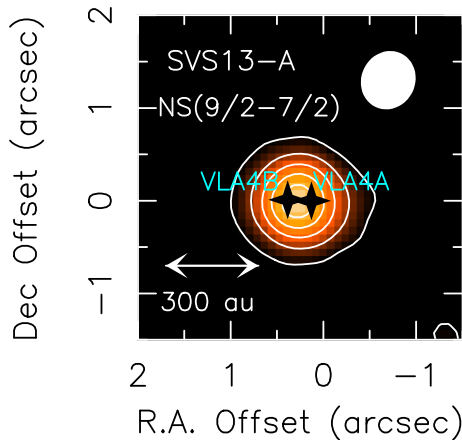


Fig. 12. Spatial distribution (contours and colour) of the SVS13-A region obtained using the NS(9/2–7/2) $\Omega = 1/2$ emission. The whole velocity emitting region has been used (from 0 km s⁻¹ to $+15$ km s⁻¹). The line profile consists of three hyperfine components, blended at the present spectral resolution (see Fig. 5 and Table 1). Angular offset are relative to the phase centre (see Sect. 3). The first contour and steps are 5σ (50 mJy km s⁻¹) and 10σ , respectively. The filled ellipse shows the synthesized beam (HPBW): $0''.65 \times 0''.58$ (PA = -46°). The black crosses indicate the positions of the VLA4A and VLA4B sources as imaged using the VLA array by Tobin et al. (2018).

0.86. Taking into account 1σ , the following constraints are derived: $T_{\text{kin}} \geq 50$ K, $n_{\text{H}_2} \geq 10^5$ cm⁻³, $N_{\text{H}_2\text{CS}} = 0.7\text{--}2 \times 10^{15}$ cm⁻², and sizes in the $0''.2\text{--}0''.8$ range.

Figure 13 shows the comparison between observations and best-fit line predictions for SO, SO₂, and H₂CS, while Table 2 summarizes the excitation ranges found for the three molecules. As a matter of fact, all the SO, SO₂, and H₂CS analysis are consistent with the occurrence of hot corino emission. This will allow us to compare the present results with what previously found using iCOMs (see Sect. 6).

For OCS, having detected three lines, two of them at very similar upper level excitation (16 K and 21 K), we did not apply

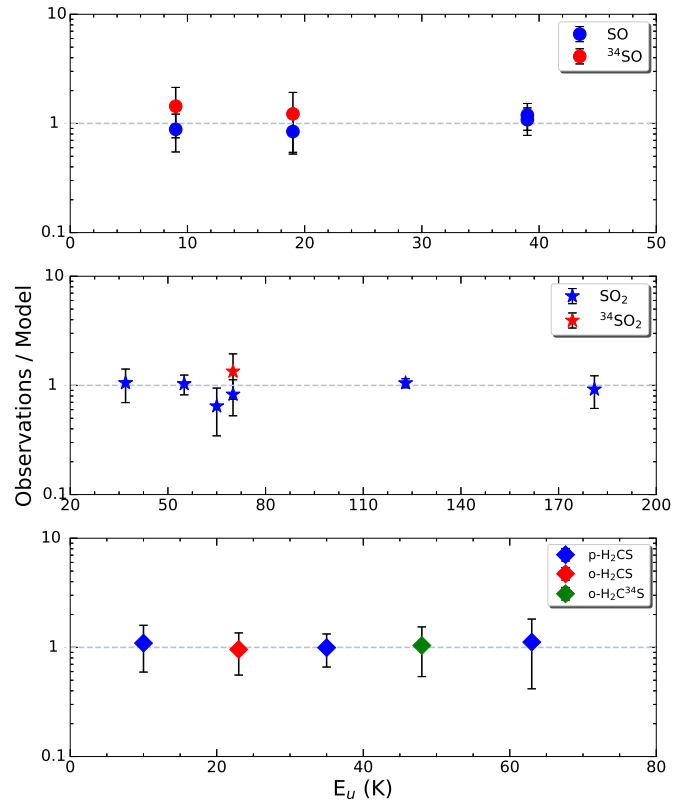


Fig. 13. Ratio of the observed and best-fit theoretical line integrated intensities of SO (upper panel), SO₂ (middle), and H₂CS (bottom) as a function of the line upper-level energy (see the text and Table 2). Different symbols indicate different isotopologues as well as ortho and para species.

the LVG analysis, adopting instead the rotational diagram (RD) approach, where LTE population and optically thin lines are assumed. Under these assumptions, for a given molecule, the relative population distribution of all the energy levels, is described

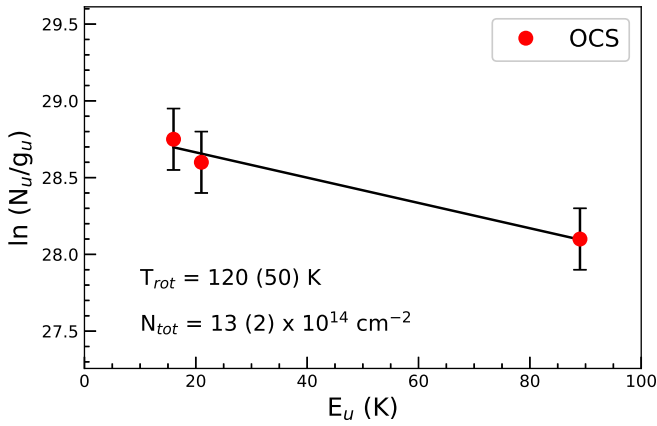


Fig. 14. Rotational diagrams for OCS derived using the emission lines observed towards SVS13-A (see Table 1 and Fig. 9). The parameters N_u , g_u , and E_{up} are, respectively, the column density, the degeneracy, and the energy (with respect to the ground state of each symmetry) of the upper level. A source size of $0''.3$ has been assumed, following the SO, SO $_2$, and H $_2$ CS LVG analysis. The derived values of the rotational temperature are reported in the panels.

by a Boltzmann temperature, that is, the rotational temperature, T_{rot} . Given the OCS emission peaks towards SVS13-A and spatially unresolved (Fig. 8), we corrected the line intensities assuming a size of $0''.3$, i.e. the average size obtained from the LVG results for SO, SO $_2$, and H $_2$ CS. The RD analysis which provides a column density of $1\text{--}2 \times 10^{15}$ cm $^{-2}$, and a rotational temperature $T_{rot} = 120 \pm 50$ K (see Fig. 14).

Finally, for CS and NS, having detected only one transition, in light of the previous LVG results, we adopted again a source size of $0''.3$ and conservatively assumed the overall temperature range (37.5–300 K, see Table 2). We consequently derived: $0.8\text{--}17 \times 10^{18}$ cm $^{-2}$ for CS, and $1\text{--}6 \times 10^{15}$ cm $^{-2}$ for NS.

6. Discussion

6.1. Chemical census of the SVS13-A hot corino

The SVS13-A system has been recently subject of IRAM 30-m (ASAI: Lefloch et al. 2018) and IRAM PdBI (CALYPSO: Maury et al. 2019) observations aimed to obtain its chemical census. More specifically, Bianchi et al. (2017, 2019a) reported the analysis of a large sample of iCOMs using the ASAI single dish unbiased spectral survey: the large number of lines allowed the authors to: (i) use the LVG approach to analyze the methanol isotopologues and (ii) consequently derive the column densities of more complex organic species (CH $_3$ CHO, H $_2$ CCO, HCOOCH $_3$, CH $_3$ OCH $_3$, CH $_3$ CH $_2$ OH, NH $_2$ CHO). On the other hand, De Simone et al. (2017) and Belloche et al. (2020) used the PdBI images (synthesized beams between $0''.5$ and $1''.7$) of iCOMs emitting in selected spectral windows to derive the column densities in LTE conditions of, again, a large number of iCOMs, namely those reported by Bianchi et al. (2019a) plus C $_2$ H $_5$ CN, a-(CH $_2$ OH) $_2$, and HCOCH $_2$ OH. Both the ASAI and the CALYPSO analysis led to an emitting size, for iCOMs, of $0''.3$, perfectly consistent with what is found in the present analysis of S-bearing species (see Table 2). The column densities are also well in agreement, being different by less than a factor of 2 for all the iCOMs in common except for methanol and formamide (a factor of 3–4). Very recently, Yang et al. (2021) also reported the results of the PEACHES ALMA survey

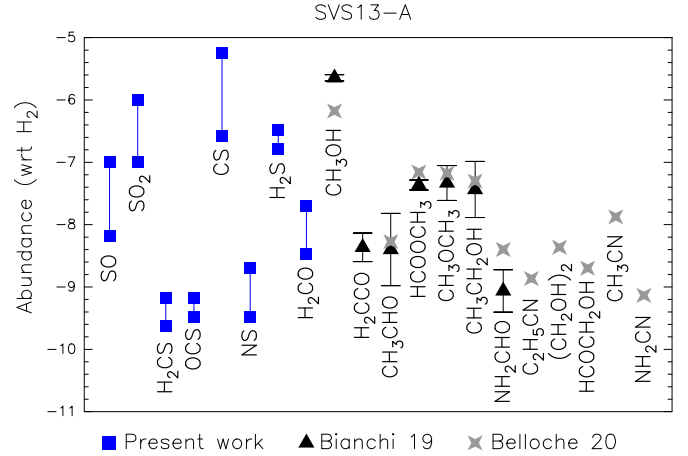


Fig. 15. Summary of the abundances with respect to H $_2$ derived for the hot corino observed towards SVS13-A (Chen et al. 2009, $N_{H_2} = 3 \times 10^{24}$ cm $^{-2}$). Blue points are for the S-species reported in the present paper, while blue triangles (Bianchi et al. 2019a) and grey diamonds (Belloche et al. 2020) are for iCOMs (see Sect. 6.1).

on the chemical content of star forming regions in Perseus, with SVS13-A among them. A large number of iCOMs have been detected in agreement with the ASAI and CALYPSO results. Column densities, in this case being of a $0''.5$ source size, are also consistent considering the uncertainties. In conclusion, once observed with a $\sim 1''$ resolution, it looks that S-bearing species are emitting from a region similar to that associated with the hot corino chemistry.

In order to derive the abundances of S-bearing species we assumed $N_{H_2} = 3 \times 10^{24}$ cm $^{-2}$ as the typical value for the inner $0''.3$ region, following what was adopted by Bianchi et al. (2019a) and Belloche et al. (2020) for the iCOMs analysis, using the continuum images by Chen et al. (2009). The abundances are reported in Table 2: the most abundant S-species are CS ($0.3\text{--}6 \times 10^{-6}$), SO ($7 \times 10^{-9}\text{--}1 \times 10^{-7}$), and SO $_2$ ($1\text{--}10 \times 10^{-7}$). On the other hand, H $_2$ CS and OCS have similar, lower, abundances (a few 10^{-10}), while $X_{NS} \sim 10^{-10}\text{--}10^{-9}$. Interestingly, the H $_2$ CS abundance in SVS13-A is four orders of magnitude higher with respect to the recently measured in the H $_2$ CS ring in the protoplanetary disk around the Class II HL Tau (Codella et al. 2020). This strongly supports the notion that sulfur chemistry is indeed definitely evolving during the star-forming process.

Finally, Fig. 15 summarizes the abundances derived here for the sulfuretted molecules as well as (i) those of iCOMs reported by Bianchi et al. (2019a) (ii) and those derived using the CALYPSO dataset De Simone et al. (2017); Belloche et al. (2020) applying the same H $_2$ column density. For completeness, we also added five-atom molecules such as H $_2$ CCO (Bianchi et al. 2019a), and CH $_3$ CN, and NH $_2$ CN (Belloche et al. 2020). The present census of the S-bearing molecules thus contribute to building up a suite of abundances representative of the inner 90 au SVS13-A region, as well as calling for modelling (beyond the scope of this paper) to constrain the chemical evolution in star-forming regions. Obviously, any theoretical approach in modelling the SVS13-A chemical richness will face the long-standing problem related to the main reservoir of sulfuretted molecules on dust mantles. A progress in that direction would surely unlock the interpretation of the chemical richness (also) around protostars. Meanwhile, a small step can be done by comparing the H $_2$ CS emission of H $_2$ CO, which is not properly an iCOM, but, instead, is a key molecule for the production of more

complex species (see e.g., Caselli & Ceccarelli 2012; Jørgensen et al. 2020, and references therein).

6.2. H_2CS versus H_2CO

One of the main reasons of astrochemical studies of protostellar regions is to understand the chemical composition of the gas where planets start their formation process. As a matter of fact, to achieve an understanding of whether planetary composition holds evidence as to where planets formed would definitely be a breakthrough (e.g., Turrini et al. 2021, and references therein). Obviously, several processes are expected to be at work to sculpt the characteristics of planetary atmospheres. Many intermediate steps would be expected to fill the gap between the interstellar chemistry and the planetary chemistry, and consequently, a complete chemical reset cannot be excluded. Whatever the path leading to planets might be, the elemental abundance ratios are the root where the atmospheric chemistry is anchored (e.g. Booth & Ilee 2019; Cridland et al. 2019, and references therein). Together with O, C, N, sulfur plays a major role in this aspect (e.g. Semenov et al. 2018; Fedele & Favre 2020; Turrini et al. 2021). Over time, the number of S-bearing species around protoplanetary disks is definitely increasing, starting with several detections of CS and SO that have been reported (e.g. Dutrey et al. 1997, 2017; Fuente et al. 2010; Guilloteau et al. 2013, 2016; Pacheco-Vázquez et al. 2016). More recently, thanks to the advent of ALMA, H_2S , H_2CS have also been imaged towards disk around Class I/II objects showing rings and gaps (Phuong et al. 2018; Le Gal et al. 2019; Codella et al. 2020; Loomis et al. 2020). These findings allow us to compare what we found for the Class I SVS13-A with more evolved star forming regions, namely Class I/II (10^5 – 10^6 yr old).

In this context, as recently remarked by Fedele & Favre (2020), the abundance ratio between H_2CS and H_2CO could be used to investigate the S/O abundance ratio provided that both molecules in the gas-phase are mainly formed by reacting O or S with the methyl group CH_3 . In order to estimate $[H_2CS]/[H_2CO]$ in SVS13-A, we used the emission of the $o\text{-}H_2CO(6_{1,5}\text{--}6_{1,6})$ transition at 101332.991 MHz ($E_u = 88$ K; from the Cologne Database for Molecular Spectroscopy (CDMS, Müller et al. 2001, 2005), falling in the present Setup 6 at 3 mm. Figure 16 reports the H_2CO spatial distribution as well as the spectrum extracted at the peak emission, both perfectly consistent with that of H_2CS as observed with the same spatial and spectral resolution (see Figs. 10 and 11). We then adopted the same size and kinetic temperature range inferred for H_2CS (see Table 2), the ortho/para ratio equal to 3 and, assuming LTE conditions, we derived a total column density $N_{H_2CO} = 2\text{--}8 \times 10^{17}$ cm $^{-2}$. The $[H_2CS]/[H_2CO]$ ratio is then between 9×10^{-4} and 2×10^{-2} .

The present values obtained for a Class I object can be compared with other measurements obtained from interferometric observations sampling Solar System scales around protostars at different evolutionary stages: (1) the prototypical Class 0 hot corino IRAS 16293-2422B as revealed with ALMA on a 60 au scale (PILS project: Jørgensen et al. 2016; Persson et al. 2018; Drozdovskaya et al. 2018, 2019): 7×10^{-4} ; (2) late Class I or II protoplanetary disks as imaged with ALMA on a 40 au scale (ALMA-DOT project: Podio et al. 2020a; Codella et al. 2020; Garufi et al. 2021): 0.1–0.2 (HL Tau) and 0.4–0.7 (IRAS 04302+2247).

The comparison suggests an increase with time of the $[H_2CS]/[H_2CO]$ ratio in the gaseous compositions around stars by more than one order of magnitude. Obviously, we cannot quantify $[S]/[O]$ from $[H_2CS]/[H_2CO]$ given the complexity of

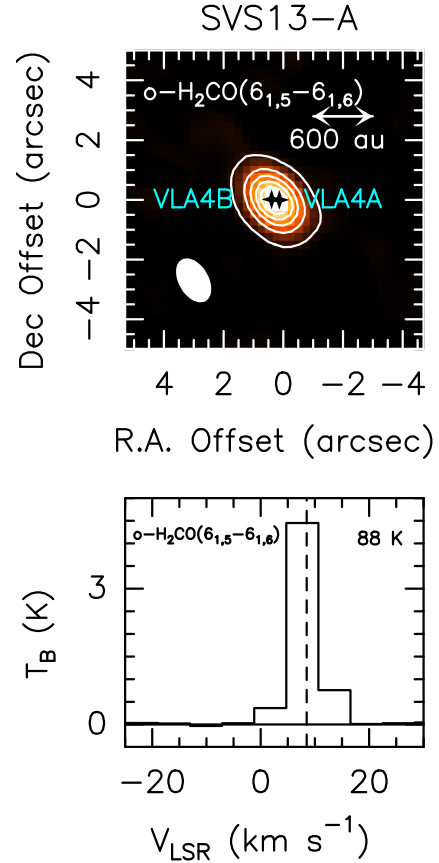


Fig. 16. H_2CO emission towards SVS13-A. *Upper panel:* spatial distribution of the $o\text{-}H_2CO(6_{1,5}\text{--}6_{1,6})$ emission. The whole velocity emitting region has been used (from -5 km s $^{-1}$ to $+20$ km s $^{-1}$). The angular offsets are relative to the phase centre (see Sect. 2). First contour and the respective steps are 5σ (25 mJy km s $^{-1}$) and 20σ , respectively. The filled ellipse shows the synthesized beam (HPBW): $1''.6 \times 1''.1$ (PA = 41°). The black crosses indicate the positions of the VLA4A and VLA4B sources as imaged using the VLA array by Tobin et al. (2018). *Lower panel:* observed $o\text{-}H_2CO(6_{1,5}\text{--}6_{1,6})$ spectrum (in T_B scale, see Table 1) extracted at the emission peak: $\alpha_{2000} = 03^h29^m03^s.75$, $\delta_{2000} = +31^\circ16'03''.8$. The upper level energy is reported. The vertical dashed line stands for the ambient LSR velocity ($+8.6$ km s $^{-1}$, Chen et al. 2009).

the overall S and O chemistry, but the present findings suggest that $[S]/[O]$ could change along the Sun-like star forming process.

Finally, we inspected what has been measured with the ROSINA spectrometer towards the comet 67P/Churyumov-Gerasimenko (C-G) in the context of the ESA Rosetta space mission Rubin et al. (2020). ROSINA derived the chemical composition of the volatiles in the coma, reporting the H_2CS and H_2CO abundance with respect to water. The corresponding $[H_2CS]/[H_2CO]$ ratio ranges in the 7×10^{-4} – 4×10^{-2} range, that is, a quite wide spread which does not allow us to verify if a relic of the early stages of our Solar System supports the tentative $[H_2CS]/[H_2CO]$ dependence on time from Class 0 to Class II objects. Clearly, more measurements are needed to perform a statistical study.

6.3. NS versus NS^+

The cation NS^+ has been very recently discovered in interstellar space using IRAM 30-m observations in the mm-spectral

window of a sample of low-mass star-forming regions (Cernicharo et al. 2018). More specifically, NS⁺ has been revealed towards cold molecular clouds and prestellar cores as well as in shocked protostellar regions and in the direction of hot corinos (e.g., NGC 1333-IRAS4A). Cernicharo et al. (2018) derived the NS/NS⁺ ratio, lying in the 30–50 range, which has been modeled according the following chemical routes (see e.g., Agúndez & Wakelam 2013): NS is formed via the reaction of SH with N or of NH with S, while NS⁺ is formed when the atomic nitrogen reacts with the SO⁺ and SH⁺ ions. On the other hand, both NS and NS⁺ should be destroyed via reactions with the O, N, or C atoms. Furthermore, NS⁺ should first go through dissociative recombination. Cernicharo et al. (2018) fit the observations by using a relatively cold gas, even for the NGC 1333-IRAS4A region ($T_{\text{kin}} \approx 30$ K), which, in turn, means that NS⁺ is not released in the hot corino, but from a more extended molecular envelope instead.

In the present SOLIS observations of SVS13-A, NS is clearly tracing the protostellar region with a source size less than 100 au, then it is plausibly emitted in the hot corino (see Fig. 12). In fact, as shown in Sect. 4, we derived the NS column density by assuming a kinetic temperature in the 50–300 K range.

Interestingly, the present SOLIS NOEMA setup covers (with a $\sim 1''.3$ spatial resolution) the frequency of the NS⁺(2–1) line (100198.55 GHz), characterized by $E_u = 7$ K, $S\mu^2 = 9$ D² (Cernicharo et al. 2018). However, this line was not detected and only an upper limit on NS⁺ column density can be derived by assuming the same emitting size as well as the same kinetic temperatures adopted for the NS analysis (see Table 2). The 3σ upper limit on the velocity integrated emission is 1 K km s^{-1} , which, in turn, allows us to fix an upper limit on $N_{\text{NH}^+} \leq 8 \times 10^{14} \text{ cm}^{-2}$. In summary, we can derive $N(\text{NS})/N(\text{NS}^+) \geq 10$, a number that is in agreement with the values reported by Cernicharo et al. (2018), in particular for the NGC 1333-IRAS4A hot corino (~ 40). We note that these findings are also consistent with the inspection of the spectra of the IRAM 30-m ASAI Legacy (Lefloch et al. 2018), which provides an unbiased spectral survey at 1, 2, and 3 mm of SVS13-A; ASAI covered not only the NS⁺(2–1) line, but also the $J = 3-2$ and $5-4$ ones, at 150295.607 MHz and 250481.463 MHz, respectively (Cernicharo et al. 2018). No detection has been found providing an upper limit on the NS⁺ column density of a few 10^{14} cm^{-2} , similarly to what was obtained with NOEMA SOLIS. The present findings, providing the first constraint on the $N(\text{NS})/N(\text{NS}^+)$ ratio based on interferometric data, call for a comparison with predictions from astrochemical modelling at work at kinetic temperatures that are typical of hot corinos (≥ 100 K).

6.4. SO versus SO₂

The importance of the SO₂ over SO abundance ratio in star forming regions has been discussed since the end of the last century. The starting assumption was that H₂S is the main S-bearing species in the dust mantles. As a consequence, the injection of the material frozen on ices due either to thermal heating (hot cores, hot corinos) or due to sputtering (shocks), or even chemical desorption caused by the excess energy of an exothermic reaction (Oba et al. 2018), increases the H₂S abundance in the gas-phase, which, in turn, first forms SO and successively SO₂ (e.g. Pineau des Forets et al. 1993; Charnley et al. 1997; Hatchell et al. 1998). As a result, [SO₂]/[SO] has been proposed as a chemical clock to date the evaporation-sputtering process. However, successive attempts to apply this tool in young ($\geq 10^3$ yr)

shocked regions was not shown to be efficient (Codella et al. 1999, 2005; Wakelam et al. 2004a), given all the uncertainties associated with the S-chemistry starting from the still open question on the main S-bearing species frozen on ices (e.g. Laas & Caselli 2019; Taquet et al. 2020, and references therein). On the other hand, a Kitt Peak single-dish (HPBW = 43'') survey of Class 0 and Class I hot corinos (10^4 – 10^5 yr) by Buckle & Fuller (2003) suggested an evolutionary trend, with [SO₂]/[SO] ≈ 0.1 for Class 0 and [SO₂]/[SO] ≈ 0.4 for Class I.

Moving on to interferometric observations, the present data set shows for the Class I SVS13-A target [SO₂]/[SO] ~ 10 , a value greater than what was measured with ALMA towards the Class 0 IRAS 16293-2422 hot corino (PILS: Drozdovskaya et al. 2018, 2019): [SO₂]/[SO] ratios ~ 3 . Both measurements are higher than what was measured using IRAM-NOEMA (in the SOLIS context) of the young shocked regions L1157 and L1448 outflows: [SO₂]/[SO] ≈ 0.2 (NGC 1333-IRAS4A Taquet et al. 2020), and 0.1–0.3 (L1157 Feng et al. 2020). In conclusion, these recent findings support the use the [SO₂]/[SO] ratio to date gas enriched in sulphur around protostars, using high-spatial interferometric images to disentangle any contributions resulting from different physical components.

6.5. On the sulfur budget in SVS13-A

The recent results by Kama et al. (2019) and Shingledecker et al. (2020) indicates that a large fraction ($\sim 90\%$) of sulphur in dense star-forming regions is found in very refractory forms such as FeS or S₈. In this context, in order to evaluate the sulfur budget in the Class I SVS13-A hot corino, we need an estimate of the abundance of H₂S, which (as reported in Sect. 1) is postulated to be a major S-bearing molecule on dust mantles. Unfortunately, the NOEMA SOLIS spectral windows do not cover H₂S line frequencies. However, the H₂S column density can be measured using the line of the para $2_{2,0}-2_{1,1}$ transition observed at 1.4 mm in the context of the IRAM 30-m ASAI Large Program (Lefloch et al. 2018). The line is emitting at 216710.4365 MHz: the HPBW is 11'' and the energy of the upper level is quite high, at 84 K^5 . This combination minimizes the contamination expected from the cold envelope with respect to the SVS13-A hot corino and excludes any possible contribution due to SVS13-B (see Fig. 1). Figure 17 reports the observed spectra, with the p-H₂S($2_{2,0}-2_{1,1}$) profile peaking at $+8.1(0.1) \text{ km s}^{-1}$, with a FWHM line width equal to $3.2(0.1) \text{ km s}^{-1}$, and an integrated area (in T_{MB} scale) of $534(14) \text{ mK km s}^{-1}$. Given $S\mu^2 = 2.1 \text{ D}^2$, assuming LTE conditions, an emitting size equal to $0''.3$, a temperature range of 50–300 K (as for the other S-species here imaged by NOEMA), and an ortho/para ratio equal to 3, we obtain a total column density of $0.5-1 \times 10^{18} \text{ cm}^{-2}$. Assuming again $N_{\text{H}_2} = 3 \times 10^{24} \text{ cm}^{-2}$ (Chen et al. 2009), the H₂S abundance result is $2-4 \times 10^{-7}$. Table 2 and Fig. 15 summarize the column density and abundances of the S-bearing molecules observed in the SVS13-A hot corino. Overall, if we take all of them into account, we reach $[\text{S}]/[\text{H}] = 3.0 \times 10^{-7}-3.8 \times 10^{-6}$, that is, 2%–17% of the Solar System [S]/[H] value (1.8×10^{-5} ; Anders & Grevesse 1989). Obviously, not all the S-species observed around low-mass protostars have been revealed in the present survey, missing mainly CCS as well as the SO⁺ and HCS⁺ ions. However, we can reasonably assume that the contribution due to CCS (a standard

⁵ The Frequencies and spectroscopic parameters have been provided by Cupp et al. (1968), Burenin et al. (1985), and Belov et al. (1995) and retrieved from the Cologne Database for Molecular Spectroscopy (Müller et al. 2001, 2005).

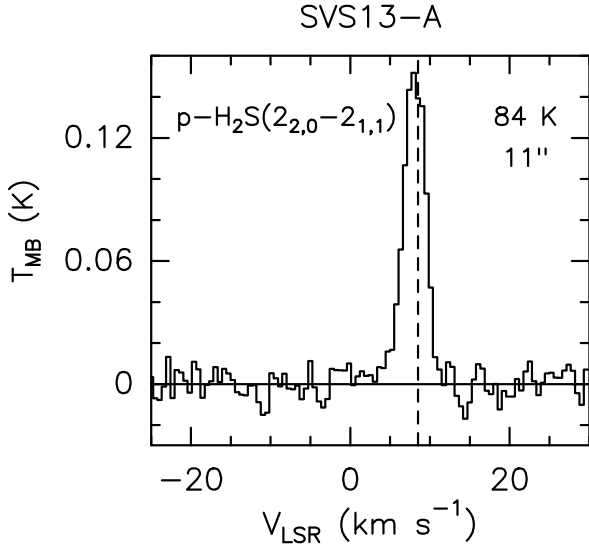


Fig. 17. Spectrum of the $p\text{-H}_2\text{S}(2_{2,0}\text{-}2_{1,1})$ line (in T_{MB} scale) as observed towards SVS13-A at 1.4 mm using the IRAM 30-m antenna. Transition and corresponding upper level energy are reported. The HPBW is also indicated. The vertical dashed line stands for the ambient LSR velocity ($+8.6 \text{ km s}^{-1}$, [Chen et al. 2009](#)).

envelope tracer) as well as the SO^+ and HCS^+ ions (two orders of magnitude less abundant than CS in the warm shocked gas in the L1157 outflow [Podio et al. 2014](#)) do not significantly contribute to the total S budget in SVS13-A.

The present measurements can be compared with what obtained in surveys of other prototypical regions associated with Sun-like star-forming regions:

The Taurus Dark Cloud TMC 1 was recently investigated in the context of the GEMS project ([Fuente et al. 2019](#)) using the IRAM 30-m and Yebes 40-m antennas in CS, SO, and HCS^+ (plus rarer isotopologues of these molecules). The authors found a strong sulfur depletion both in the translucent low-density phase (where $[\text{S}]/[\text{H}]$ is 2–12% of the Solar System one, very similar to what is found in SVS13-A) and in the dense core (where this percentage falls down to 0.4%). Additional GEMS H_2S observations, reported by [Navarro-Almáida et al. \(2020\)](#), did not significantly change these results.

The L1689N star forming region, hosting the well known Class 0 hot corinos IRAS 16293-2422A and B, was sampled using SO, and SO_2 , and H_2S as observed by [Wakelam et al. \(2004b\)](#) with the IRAM 30-m single-dish. The authors estimate, for the hot corino region, the $[\text{S}]/[\text{H}]$ ratio to be $\sim 8\%$ of the Solar System value. Successively, in the context of the PILS Large Program ([Jørgensen et al. 2016](#)), [Drozdovskaya et al. \(2018, 2019\)](#) report the census of S-bearing species as observed with ALMA towards the hot corino IRAS 16293-2422B (SO, SO_2 , H_2S , CS, H_2CS , and CH_3SH). Assuming an H_2 column density of 10^{25} cm^{-2} derived in the PILS context by [Jørgensen et al. \(2016\)](#), the $[\text{S}]/[\text{H}]$ ratio is then $\sim 1\%$ of the Solar System measurement.

[Holdship et al. \(2019\)](#) measured the sulfur budget in the $\sim 100 \text{ K}$ shocked regions associated with the protostellar L1157 jet. In this case, the sampled region is chemically enriched due to sputtering and shuttering induced by a shock with a velocity of $\approx 20\text{--}40 \text{ km s}^{-1}$ (e.g., [Flower et al. 2010](#); [Viti et al. 2011](#)). For the bright L1157-B1 shock, [Holdship et al. \(2019\)](#) report $[\text{S}]/[\text{H}] \sim 10\%$ of the Solar System, which is in agreement with that found for SVS13-A.

In summary, the given percentages of the $[\text{S}]/[\text{H}]$ value with respect to the Solar System value are: 0.4% (dense core), 1–8% (Class 0 object), 2–17% (Class I object), 10% (shock). Obviously, these estimates are strongly dependent on the uncertainties associated with the adopted H_2 column densities. For instance [Jørgensen et al. \(2016\)](#) use $N(\text{H}_2) = 10^{25} \text{ cm}^{-2}$ for IRAS 16293-2422B, while [Bianchi et al. \(2019a\)](#) and [Belloche et al. \(2020\)](#) adopt $3 \times 10^{24} \text{ cm}^{-2}$ for SVS13-A. With these caveats in mind, we can speculate that (1) the increase of S-bearing molecules in the gas-phase due to thermal evaporation in a Class 0 hot corino seems to remain constant in the more evolved Class I stage as well; (2) the enrichment of sulfuretted molecules (with respect to dense cold clouds) due to thermal evaporation seems to be quantitatively the same as that in shocks, where sputtering dominates.

7. Summary and conclusions

In the context of the IRAM NOEMA SOLIS Large Program, we observed the SVS13-A Class I object at both 3 mm (beam $\approx 1''.5$) and 1.4 mm (beam $\approx 0''.6$) in order to obtain a census of the S-bearing species. The main results can be summarized as follows:

- We obtained 32 images of emission lines of ^{32}SO , ^{34}SO , C^{32}S , C^{34}S , C^{33}S , OCS, $\text{H}_2\text{C}^{32}\text{S}$, $\text{H}_2\text{C}^{34}\text{S}$, and NS, sampling E_u up to 244 K. The low-excitation (9 K) SO is peaking towards SVS13-A. This emission also traces the molecular envelope and the low-velocity outflow emission driven by SVS13-A. In addition, SO images the collimated high-velocity (up to 100 km s^{-1} shifted with respect to the systemic velocity) jet driven by the nearby SVS13-B Class 0. In general, the molecular envelope contributes to the low-excitation (less than 40 K) SO and CS emission. Conversely, all the rest of the observed species and transitions show a compact emission around the SVS13-A coordinates indicating the inner $\sim 100 \text{ au}$ protostellar region.
- The non-LTE LVG analysis of SO, SO_2 , and H_2CS indicates a hot corino origin. The emitting size is about 90 au (SO), 60 au (SO_2), and 120 au (H_2CS). For SO, we have $T_{\text{kin}} \geq 150 \text{ K}$, and $n_{\text{H}_2} \geq 6 \times 10^6 \text{ cm}^{-3}$. The analysis of SO_2 leads $T_{\text{kin}} \approx 100\text{--}300 \text{ K}$, and $n_{\text{H}_2} \geq 5 \times 10^6 \text{ cm}^{-3}$. Finally, for H_2CS , $T_{\text{kin}} \geq 50 \text{ K}$, and $n_{\text{H}_2} \geq 10^5 \text{ cm}^{-3}$. For OCS, we used the rotation diagram approach using LTE obtaining a T_{rot} of $120 \pm 50 \text{ K}$, which is consistent with the temperatures expected for a hot corino.
- The bright emission from S-bearing molecules is confirmed to arise from the SVS13-A hot corino, where the iCOMs, previously imaged, are abundant [De Simone et al. \(2017\)](#); [Bianchi et al. \(2019a\)](#); [Belloche et al. \(2020\)](#). The abundances of the sulphuretted species are in the following ranges: $0.3\text{--}6 \times 10^{-6}$ (CS), $0.7\text{--}10 \times 10^{-7}$ (SO), $1\text{--}10 \times 10^{-7}$ (SO_2), a few 10^{-10} (H_2CS and OCS), and $10^{-10}\text{--}10^{-9}$ (NS).
- Also NS is tracing a region with a size less than 100 au. We constrain for the first time the $\text{N}(\text{NS})/\text{N}(\text{NS}^+)$ using interferometric observations: ≥ 10 . This is in agreement with what is previously reported for the NGC 1333-IRAS4A hot corino by [Cernicharo et al. \(2018\)](#) using single-dish measurements, supporting that NS^+ is mainly formed in the extended envelope.
- Once measured using the NOEMA array, the $[\text{SO}_2]/[\text{SO}]$ ratio towards SVS13-A is ~ 10 , a value slightly larger (by a factor 3) than what was measured with ALMA towards the

Class 0 IRAS 16293-2422B hot corino (PILS: Drozdovskaya et al. 2018, 2019). This is clearly not enough to support the use of the $[\text{SO}_2]/[\text{SO}]$ as chemical clock. However, after several unsuccessful attempts done in the past using observations sampling gas on large scales (mainly using single-dish antennas), the present measurements suggest to verify the use of $[\text{SO}_2]/[\text{SO}]$ as chemical clock, but sampling the inner 100 au around the protostars.

- Considering that in the gas-phase H_2CS and H_2CO (i) are mainly formed by reacting O or S with the methyl group CH_3 , and (ii) they are among the few species detected from protostars to protoplanetary disks, we derived their abundance ratio in SVS13-A, obtaining $0.9 \times 10^{-3} - 2 \times 10^{-2}$. The comparison between the few interferometric observations sampling Solar System scales (IRAS 16293-2422B, SVS13-A, HL Tau, and IRAS 04302+2247) suggests an increase with time of the $[\text{H}_2\text{CS}]/[\text{H}_2\text{CO}]$ ratio in the gaseous compositions around stars by more than one order of magnitude. It is then tempting to speculate that $[\text{S}]/[\text{O}]$ could vary along the Sun-like star forming process.
- The estimate of the $[\text{S}]/[\text{H}]$ budget in SVS13-A is 2%–17% of the Solar System value (1.8×10^{-5}). This number is consistent with what was previously measured towards Class 0 objects (1%–8%). As a matter of fact, it seems that the enrichment of the S-bearing molecules in Class 0 hot corinos (with respect to dense and cold clouds) remain in the Class I stage.

To conclude, the present results are in agreement with the results reported by Kama et al. (2019), who analyzed a sample of young stars photospheres, concluding that $89\% \pm 8\%$ of elemental sulfur in their disks is locked in refractory form. Kama et al. (2019) conclude that the main S-carrier in the dust has to be more refractory than water, suggesting sulfide minerals such as FeS. Note also that recently (Shingledecker et al. 2020) have shown that radiation chemistry converts a large fraction of S in allotropic form, in particular S_8 , which cannot be detected (except for possible desorption products due to photo-processes or shocks, such as S_2 , S_3 , and S_4 , as also detected in the coma of the 67P/Churyumov-Gerasimenko comet (Calmonte et al. 2016). Indeed, this is supported by the fact that even in a shocked region such as L1157-B1, associated with both C and J-shocks (Benedettini et al. 2012) and indeed rich in water ($\text{H}_2\text{O}/\text{H}_2 = 10^{-4}$; Busquet et al. 2014), the $[\text{S}]/[\text{H}]$ ratio is not significantly greater than what has been found for both Class 0 and Class I hot corinos.

Acknowledgements. We thank the referee M. Drozdovskaya for her careful and instructive report, that definitely improved the manuscript. We are also very grateful to all the IRAM staff, whose dedication allowed us to carry out the SOLIS project. This work was supported by (i) the European Marie Skłodowska-Curie Actions under the European Union's Horizon 2020 research and innovation programme, for the Project "Astro-Chemistry Origins" (ACO), Grant No 811312, (ii) the European Research Council (ERC) under the European Union's Horizon 2020 research and innovation programme, for the Project "The Dawn of Organic Chemistry" (DOC), grant agreement No 741002, and (iii) the project PRIN-INAF 2016 The Cradle of Life - GENESIS-SKA (General Conditions in Early Planetary Systems for the rise of life with SKA). This work is also supported by the French National Research Agency in the framework of the Investissements d'Avenir program (ANR-15-IDEX-02), through the funding of the "Origin of Life" project of the Univ. Grenoble-Alpes.

References

Agúndez, M., & Wakelam, V. 2013, *Chem. Rev.*, 113, 8710
 Anders, E., & Grevesse, N. 1989, *Geochim. Cosmochim. Acta*, 53, 197
 Andrews, S. M., Huang, J., Pérez, L. M., et al. 2018, *ApJ*, 869, L41
 Anglada, G., Rodríguez, L. F., & Torrelles, J. M. 2000, *ApJ*, 542, L123

Bachiller, R., Guilloteau, S., Gueth, F., et al. 1998, *A&A*, 339, L49
 Bachiller, R., Pérez Gutiérrez, M., Kumar, M. S. N., & Tafalla, M. 2001, *A&A*, 372, 899
 Balança, C., Spielfiedel, A., & Feautrier, N. 2016, *MNRAS*, 460, 3766
 Belloche, A., Maury, A. J., Maret, S., et al. 2020, *A&A*, 635, A198
 Belov, S. P., Yamada, K. M. T., Winniewisser, G., et al. 1995, *J. Mol. Spectr.*, 173, 380
 Benedettini, M., Busquet, G., Lefloch, B., et al. 2012, *A&A*, 539, A3
 Bergner, J. B., Öberg, K. I., Garrod, R. T., & Graninger, D. M. 2017, *ApJ*, 841, 120
 Bergner, J. B., Martín-Doménech, R., Öberg, K. I., et al. 2019, *ACS Earth Space Chem.*, 3, 1564
 Bianchi, E., Codella, C., Ceccarelli, C., et al. 2017, *MNRAS*, 467, 3011
 Bianchi, E., Ceccarelli, C., Codella, C., et al. 2019a, *ACS Earth Space Chem.*, 3, 2659
 Bianchi, E., Codella, C., Ceccarelli, C., et al. 2019b, *MNRAS*, 483, 1850
 Bianchi, E., Chandler, C. J., Ceccarelli, C., et al. 2020, *MNRAS*, 498, L87
 Bogey, M., Demuynck, C., & Destombes, J. L. 1981, *Chem. Phys. Lett.*, 81, 256
 Boogert, A. C. A., Gerakines, P. A., & Whittet, D. C. B. 2015, *ARA&A*, 53, 541
 Booth, R. A., & Ilee, J. D. 2019, *MNRAS*, 487, 3998
 Booth, A. S., Walsh, C., Kama, M., et al. 2018, *A&A*, 611, A16
 Buckle, J. V., & Fuller, G. A. 2003, *A&A*, 399, 567
 Burenin, A. V., Fevral'skikh, T. M., Mel'nikov, A. A., & Shapin, S. M. 1985, *J. Mol. Spectro.*, 109, 1
 Busquet, G., Lefloch, B., Benedettini, M., et al. 2014, *A&A*, 561, A120
 Calmonte, U., Altwegg, K., Balsiger, H., et al. 2016, *MNRAS*, 462, S253
 Caselli, P., & Ceccarelli, C. 2012, *A&ARv*, 20, 56
 Ceccarelli, C., Maret, S., Tielens, A. G. G. M., Castets, A., & Caux, E. 2003, *A&A*, 410, 587
 Ceccarelli, C., Caselli, P., Herbst, E., Tielens, A. G. G. M., & Caux, E. 2007, *Protostars and Planets V*, 47
 Ceccarelli, C., Caselli, P., Fontani, F., et al. 2017, *ApJ*, 850, 176
 Cernicharo, J., Lefloch, B., Agúndez, M., et al. 2018, *ApJ*, 853, L22
 Charnley, S. B., Tielens, A. G. G. M., & Rodgers, S. D. 1997, *ApJ*, 482, L203
 Chen, X., Launhardt, R., & Henning, T. 2009, *ApJ*, 691, 1729
 Chini, R., Reipurth, B., Sievers, A., et al. 1997, *A&A*, 325, 542
 Codella, C., Bachiller, R., & Reipurth, B. 1999, *A&A*, 343, 585
 Codella, C., Bachiller, R., Benedettini, M., et al. 2005, *MNRAS*, 361, 244
 Codella, C., Ceccarelli, C., Cabrit, S., et al. 2016, *A&A*, 586, A3
 Codella, C., Podio, L., Garufi, A., et al. 2020, *A&A*, 644, A120
 Cridland, A. J., van Dishoeck, E. F., Alessi, M., & Pudritz, R. E. 2019, *A&A*, 632, A63
 Cupp, R. E., Kempf, R. A., & Gallagher, J. J. 1968, *Phys. Rev.*, 171, 60
 De Simone, M., Codella, C., Testi, L., et al. 2017, *A&A*, 599, A121
 Dionatos, O., Kristensen, L. E., Tafalla, M., Güdel, M., & Persson, M. 2020, *A&A*, 641, A36
 Drozdovskaya, M. N., van Dishoeck, E. F., Jørgensen, J. K., et al. 2018, *MNRAS*, 476, 4949
 Drozdovskaya, M. N., van Dishoeck, E. F., Rubin, M., Jørgensen, J. K., & Altwegg, K. 2019, *MNRAS*, 490, 50
 Dubernet, M.-L., Alexander, M. H., Ba, Y. A., et al. 2013, *A&A*, 553, A50
 Dutrey, A., Guilloteau, S., & Guélin, M. 1997, *A&A*, 317, L55
 Dutrey, A., Guilloteau, S., Piétu, V., et al. 2017, *A&A*, 607, A130
 Fedele, D., & Favre, C. 2020, *A&A*, 638, A110
 Fedele, D., Tazzari, M., Booth, R., et al. 2018, *A&A*, 610, A24
 Feng, S., Codella, C., Ceccarelli, C., et al. 2020, *ApJ*, 896, 37
 Flower, D. R., Pineau des Forêts, G., & Rabli, D. 2010, *MNRAS*, 409, 29
 Fuente, A., Cernicharo, J., Agúndez, M., et al. 2010, *A&A*, 524, A19
 Fuente, A., Navarro, D. G., Caselli, P., et al. 2019, *A&A*, 624, A105
 Garufi, A., Podio, L., Codella, C., et al. 2020, *A&A*, 636, A65
 Garufi, A., Podio, L., Codella, C., et al. 2021, *A&A*, 645, A145
 Guilloteau, S., Di Folco, E., Dutrey, A., et al. 2013, *A&A*, 549, A92
 Guilloteau, S., Reboussin, L., Dutrey, A., et al. 2016, *A&A*, 592, A124
 Hatchell, J., Thompson, M. A., Millar, T. J., & MacDonald, G. H. 1998, *A&A*, 338, 713
 Herbst, E., & van Dishoeck, E. F. 2009, *ARA&A*, 47, 427
 Holdship, J., Viti, S., Jimenez-Serra, I., et al. 2016, *MNRAS*, 463, 802
 Holdship, J., Jimenez-Serra, I., Viti, S., et al. 2019, *ApJ*, 878, 64
 Imai, M., Sakai, N., Oya, Y., et al. 2016, *ApJ*, 830, L37
 Jørgensen, J. K., van der Wiel, M. H. D., Coutens, A., et al. 2016, *A&A*, 595, A117
 Jørgensen, J. K., Belloche, A., & Garrod, R. T. 2020, *ARA&A*, 58, 727
 Kama, M., Shorttle, O., Jermyn, A. S., et al. 2019, *ApJ*, 885, 114
 Laas, J. C., & Caselli, P. 2019, *A&A*, 624, A108
 Le Gal, R., Öberg, K. I., Loomis, R. A., Pegues, J., & Bergner, J. B. 2019, *ApJ*, 876, 72
 Le Gal, R., Öberg, K. I., Huang, J., et al. 2020, *ApJ*, 898, 131

- Lee, S. K., Ozeki, H., & Saito, S. 1995, *ApJS*, **98**, 351
- Lefèvre, C., Cabrit, S., Maury, A. J., et al. 2017, *A&A*, **604**, L1
- Lefloch, B., Castets, A., Cernicharo, J., Langer, W. D., & Zylka, R. 1998, *A&A*, **334**, 269
- Lefloch, B., Ceccarelli, C., Codella, C., et al. 2017, *MNRAS*, **469**, L73
- Lefloch, B., Bachiller, R., Ceccarelli, C., et al. 2018, *MNRAS*, **477**, 4792
- Lique, F., Senent, M. L., Spielfiedel, A., & Feautrier, N. 2007, *J. Chem. Phys.*, **126**, 164312
- Loomis, R. A., Öberg, K. I., Andrews, S. M., et al. 2020, *ApJ*, **893**, 101
- Looney, L. W., Mundy, L. G., & Welch, W. J. 2000, *ApJ*, **529**, 477
- Lovas, F. J. 2004, *J. Phys. Chem. Ref. Data*, **33**, 177
- Maury, A. J., André, P., Testi, L., et al. 2019, *A&A*, **621**, A76
- Müller, H. S. P., Thorwirth, S., Roth, D. A., & Winnewisser, G. 2001, *A&A*, **370**, L49
- Müller, H. S. P., Schlöder, F., Stutzki, J., & Winnewisser, G. 2005, *J. Mol. Struct.*, **742**, 215
- Navarro-Almaida, D., Le Gal, R., Fuente, A., et al. 2020, *A&A*, **637**, A39
- Oba, Y., Tomaru, T., Lamberts, T., Kouchi, A., & Watanabe, N. 2018, *Nat. Astron.*, **2**, 228
- Öberg, K. I., Lauck, T., & Graninger, D. 2014, *ApJ*, **788**, 68
- Oya, Y., & Yamamoto, S. 2020, *ApJ*, **904**, 185
- Pacheco-Vázquez, S., Fuente, A., Baruteau, C., et al. 2016, *A&A*, **589**, A60
- Persson, M. V., Jørgensen, J. K., Müller, H. S. P., et al. 2018, *A&A*, **610**, A54
- Phuong, N. T., Chapillon, E., Majumdar, L., et al. 2018, *A&A*, **616**, L5
- Pickett, H. M., Poynter, R. L., Cohen, E. A., et al. 1998, *J. Quant. Spec. Radiat. Transf.*, **60**, 883
- Pineau des Forets, G., Roueff, E., Schilke, P., & Flower, D. R. 1993, *MNRAS*, **262**, 915
- Podio, L., Lefloch, B., Ceccarelli, C., Codella, C., & Bachiller, R. 2014, *A&A*, **565**, A64
- Podio, L., Garufi, A., Codella, C., et al. 2020a, *A&A*, **642**, L7
- Podio, L., Garufi, A., Codella, C., et al. 2020b, *A&A*, **644**, A119
- Podio, L., Tabone, B., Codella, C., et al. 2021, *A&A*, **648**, A45
- Reipurth, B., Chini, R., Krugel, E., Kreysa, E., & Sievers, A. 1993, *A&A*, **273**, 221
- Rubin, M., Engrand, C., Snodgrass, C., et al. 2020, *Space Sci. Rev.*, **216**, 102
- Sakai, N., Oya, Y., Sakai, T., et al. 2014a, *ApJ*, **791**, L38
- Sakai, N., Sakai, T., Hirota, T., et al. 2014b, *Nature*, **507**, 78
- Schöier, F. L., van der Tak, F. F. S., van Dishoeck, E. F., & Black, J. H. 2005, *A&A*, **432**, 369
- Scoville, N. Z., & Solomon, P. M. 1974, *ApJ*, **187**, L67
- Semenov, D., Favre, C., Fedele, D., et al. 2018, *A&A*, **617**, A28
- Sheehan, P. D., & Eisner, J. A. 2017, *ApJ*, **851**, 45
- Shingledecker, C. N., Lamberts, T., Laas, J. C., et al. 2020, *ApJ*, **888**, 52
- Sperling, T., Eisloffel, J., Fischer, C., et al. 2020, *A&A*, **642**, A216
- Taquet, V., Codella, C., De Simone, M., et al. 2020, *A&A*, **637**, A63
- Teague, R., Henning, T., Guilloteau, S., et al. 2018, *ApJ*, **864**, 133
- Tieftrunk, A., Pineau des Forets, G., Schilke, P., & Walmsley, C. M. 1994, *A&A*, **289**, 579
- Tobin, J. J., Looney, L. W., Li, Z.-Y., et al. 2016, *ApJ*, **818**, 73
- Tobin, J. J., Looney, L. W., Li, Z.-Y., et al. 2018, *ApJ*, **867**, 43
- Turrini, D., Schisano, E., Fonte, S., et al. 2021, *ApJ*, **909**, 40
- van 't Hoff, M. L. R., van Dishoeck, E. F., Jørgensen, J. K., & Calcutt, H. 2020, *A&A*, **633**, A7
- Viti, S., Jimenez-Serra, I., Yates, J. A., et al. 2011, *ApJ*, **740**, L3
- Wakelam, V., Caselli, P., Ceccarelli, C., Herbst, E., & Castets, A. 2004a, *A&A*, **422**, 159
- Wakelam, V., Castets, A., Ceccarelli, C., et al. 2004b, *A&A*, **413**, 609
- Wiesenfeld, L., & Faure, A. 2013, *MNRAS*, **432**, 2573
- Wilson, T. L., & Rood, R. 1994, *ARA&A*, **32**, 191
- Yang, Y.-L., Sakai, N., Zhang, Y., et al. 2021, *ApJ*, **910**, 20
- Zucker, C., Schlafly, E. F., Speagle, J. S., et al. 2018, *ApJ*, **869**, 83

Appendix A: Comparison between NOEMA-SOLIS and IRAM 30m-ASAI

Figures A.1 and A.2 show the comparison between the IRAM 30-m 1.4mm and 3mm spectrum obtained in the context of the ASAI Large Program (Lefloch et al. (2018)) and the spectra derived by integrating the emission in the NOEMA-SOLIS images in a region equal to the HPBW of the IRAM 30-m. The output is clearly different, with the single-dish observations collecting not only the emission imaged with NOEMA (LAS $\approx 8''-9''$), but also the large-scale structure (e.g., molecular envelope around SVS13-A, extended outflow.). More specifically, Figs. A.3 and A.4 report zoomed-in portions of the 3mm and 1.4mm spectra to enlight lines of selected S-bearing molecules. The comparison confirms that, as expected, the NOEMA-SOLIS maps are well suited to image hot corinos. A particular case is represented by the SO single-dish spectra, which collect a considerable amount of flux due to extended emission. On the other hand, the lines attributed to SO₂ and H₂CS, for instance, are less affected by emission filtering.

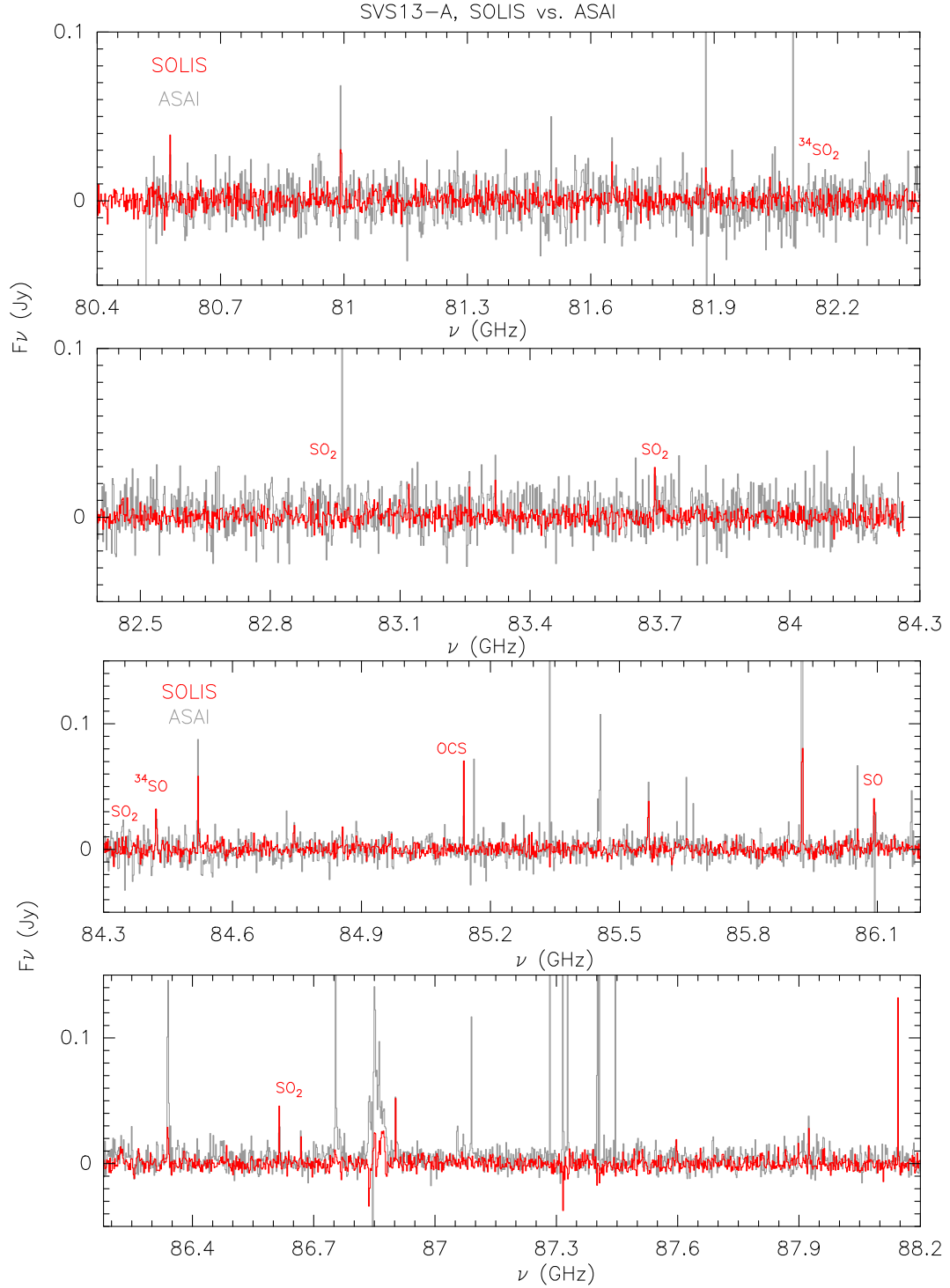


Fig. A.1. Comparison (in flux density scale) of the 3mm spectrum as observed using the IRAM 30-m antenna (grey; in the ASAI LP context [Lefloch et al. \(2018\)](#)) and that extracted from the present NOEMA SOLIS maps (red) from a circular region equal to the IRAM 30-m HPBW (24'' at 104 GHz, 31'' at 80 GHz). The ASAI spectrum has been smoothed to match the SOLIS velocity resolution (2 MHz, see Sect. 2). Red labels indicate the S-bearing species analyzed in this paper (see Table 1).

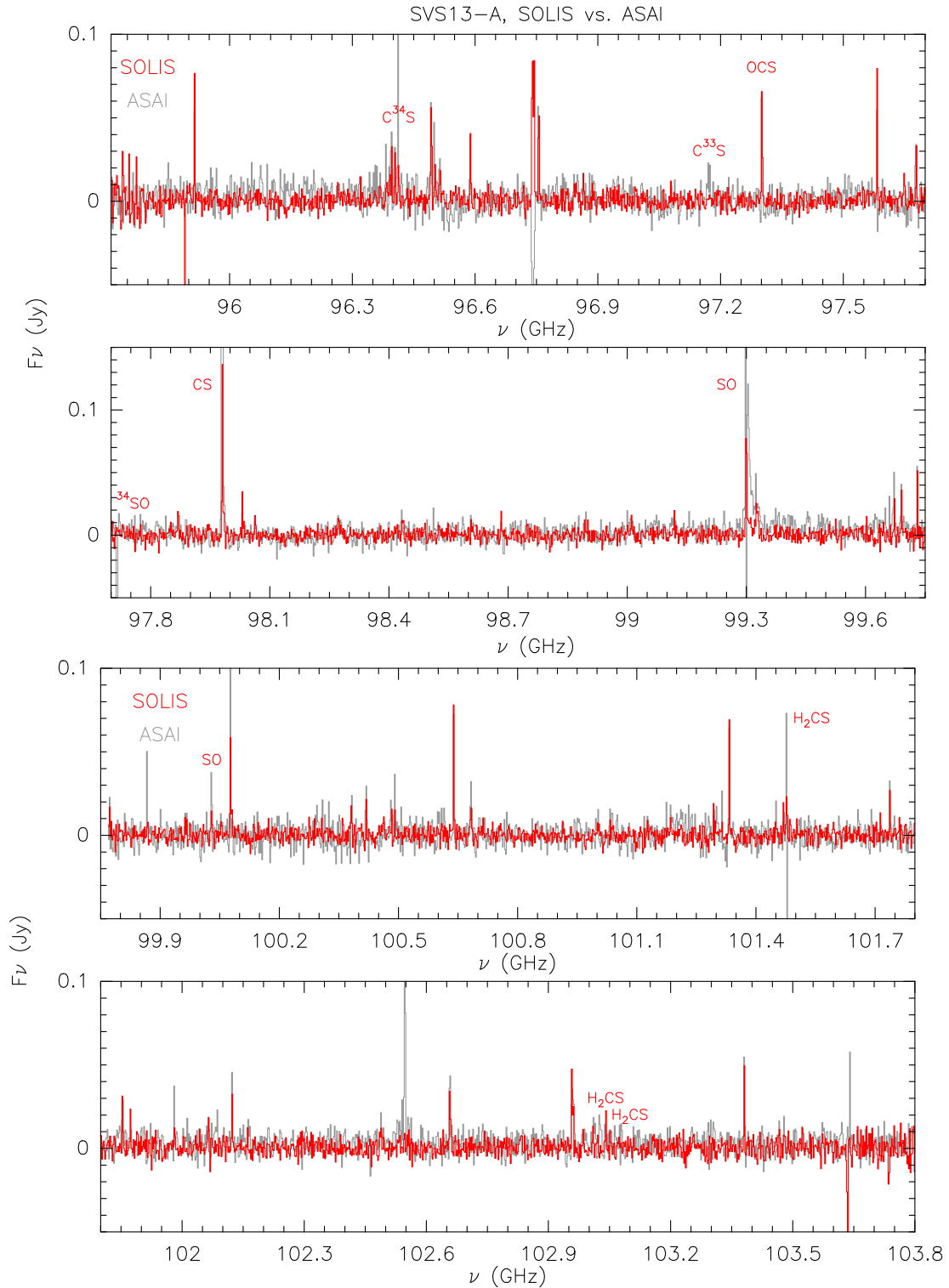


Fig. A.1. *Continued.* Comparison (in flux density scale) of the 3mm spectrum as observed using the IRAM 30-m antenna (grey; in the ASAI LP context [Lefloch et al. \(2018\)](#)) and that extracted from the present NOEMA SOLIS maps (red) from a circular region equal to the IRAM 30-m HPBW (24'' at 104 GHz, 31'' at 80 GHz). The ASAI spectrum has been smoothed to match the SOLIS velocity resolution (2 MHz, see Sect. 3). Red labels indicate the S-bearing species analyzed in this paper (see Table 1).

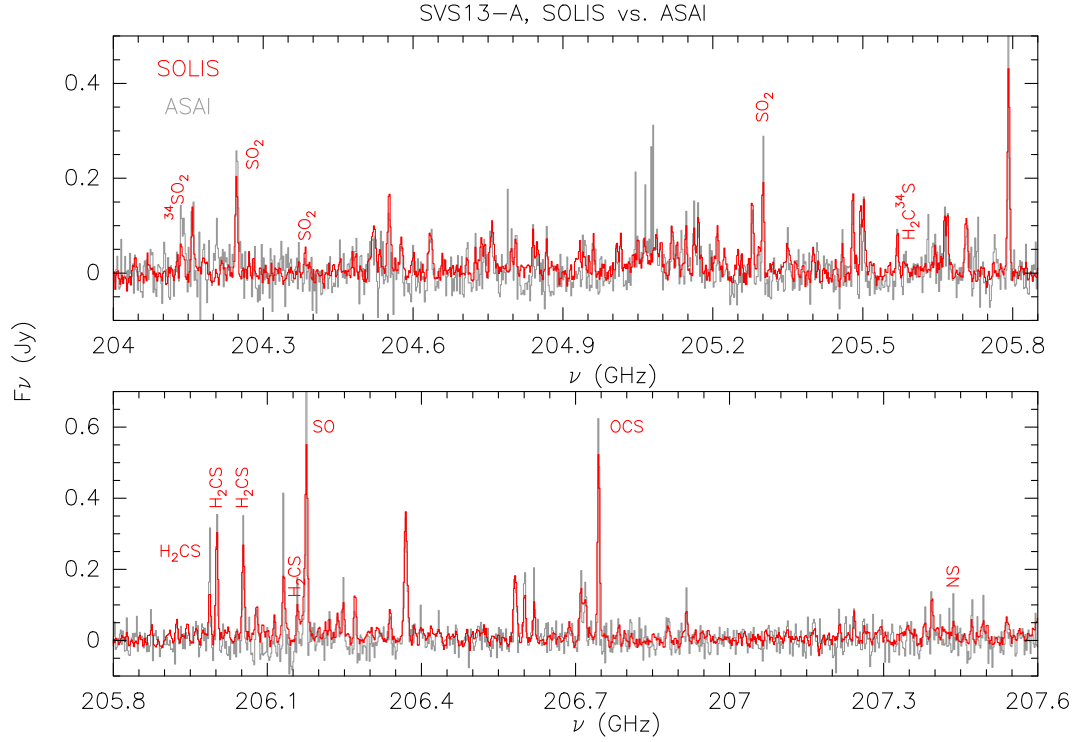


Fig. A.2. Comparison (in flux density scale) of the 1.4mm spectrum as observed using the IRAM 30-m antenna (grey; in the ASAI LP context [Lefloch et al. \(2018\)](#)) and that extracted from the present NOEMA SOLIS maps (red) from a circular region equal to the IRAM 30-m HPBW (12"). The ASAI spectrum has been smoothed to match the SOLIS velocity resolution (2 MHz, see Sect. 3). Red labels indicate the S-bearing species analyzed in this paper (see Table 1).

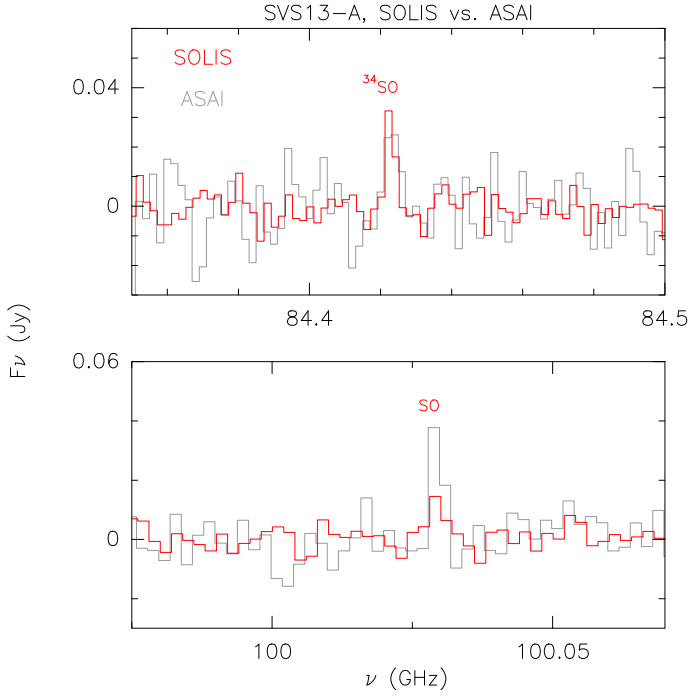


Fig. A.3. Zoom-in of Fig. A.1 to enlight selected emission lines of S-bearing species: Comparison (in flux density scale) of the 3mm spectrum as observed using the IRAM 30-m antenna (grey; in the ASAI LP context [Lefloch et al. \(2018\)](#)) and that extracted from the present NOEMA SOLIS maps (red) from a circular region equal to the IRAM 30-m HPBW (25'' at 100 GHz, 29'' at 84 GHz). The ASAI spectrum has been smoothed to match the SOLIS velocity resolution (2 MHz, see Sect. 3). Red labels indicate the S-bearing species analyzed in this paper (see Table 1).

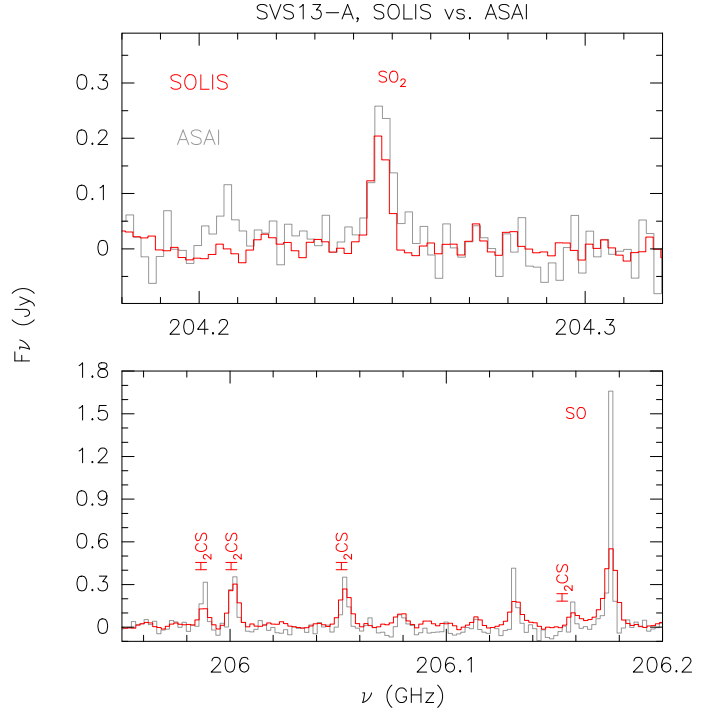


Fig. A.4. Zoom-in of Fig. A.2 to enlight selected emission lines of S-bearing species: Comparison (in flux density scale) of the 1.4mm spectrum as observed using the IRAM 30-m antenna (grey; in the ASAI LP context [Lefloch et al. \(2018\)](#)) and that extracted from the present NOEMA SOLIS maps (red) from a circular region equal to the IRAM 30-m HPBW (12''). The ASAI spectrum has been smoothed to match the SOLIS velocity resolution (2 MHz, see Sect. 3). Red labels indicate the S-bearing species analyzed in this paper (see Table 1).